

TECHNICAL NOTE

D-1665

NUMERICAL EVALUATION OF ION-THRUSTOR OPTICS

By Vladimir Hamza and Edward A. Richley

Lewis Research Center
Cleveland, Ohio

NATIONAL AERONAUTICS AND SPACE ADMINISTRATION
WASHINGTON

May 1963

554478

52P

42p
N63-15767
code 1

NATIONAL AERONAUTICS AND SPACE ADMINISTRATION

TECHNICAL NOTE D-1665

NUMERICAL EVALUATION OF ION-THRUSTOR OPTICS

By Vladimir Hamza and Edward A. Richley

SUMMARY

15767

A numerical solution of the two-dimensional Poisson equation with mixed boundary conditions is presented. Examples of analysis of four variations in an electrostatic thruster configuration are included, and results are compared.

Solution of the matrix equation (obtained from finite difference equations) by the Cyclic Chebyshev Semi-Iterative method is described along with the effect of the relaxation factor on the rate of convergence. An estimate of the space-charge-density function is first obtained from the Laplacian potential distribution and the equations of motion. The solution of the Poisson equation is then accomplished by a method of successive approximations. A suppression-factor method of dealing with the typical problem of overestimation of the first-order space-charge-density function is discussed.

A portion of the program of particular interest is the space-charge-limited current calculation. This calculation is discussed in detail, and the accuracy of the solution is compared with analytical results for flow between concentric cylinders.

The thruster configuration chosen for study is a symmetrical multimodular array of the contact-ionization closely spaced grid electrode type. Four modular designs having similar electrode configurations but different ion-emitter contours are analyzed, and the effects of focusing, electrode spacing, and grid-wire diameter are compared.

Results show that a partly blocked, curved ion emitter gives the best performance in terms of maximum percent ion transmission and low beam spreading for a given beam power. Simplicity and ease of fabrication are important considerations for any practical design. In this respect, a flat ion emitter with a focusing electrode can give good performance in terms of ion transmission and beam spreading.

Finally, the results of the analysis are compared with data obtained from an experimental thruster.

INTRODUCTION

The potential uses and relative merits of ion thrusters for future space-

flight applications are well recognized. In many instances, the thruster must exhibit capability of long operating life as well as high overall efficiency. Near-perfect ion optics, to minimize accelerator sputtering, thus becomes a major requirement of ion thruster design.

A method of analysis of the ion optics of a thruster design is discussed herein. The material presented is an extension of the work described in reference 1. The method of analysis consists of a numerical solution of the space-charge-flow problem, that is, the solution of the two-dimensional Poisson equation and the equations of motion. This method is demonstrated in reference 1 for a closely spaced grid electrode ion thruster with a flat ion emitter. A contoured ion emitter is one possible approach toward improved ion optics. Extension of the method of reference 1 to include contoured ion emitters is presented herein, and the accuracy of the method is compared with known analytic solutions for the flow between concentric cylinders. The extension to include contoured ion-emitter geometries required thorough investigation of the influence of certain parameters on the accuracy of the overall solution of the Poisson equation. As a result, the program has now effectively been generalized to the extent that it is capable of solving the space-charge-flow problem of practically any two-dimensional electrostatic thruster configuration. Solutions are obtained on an IBM 7090 computer.

As an application of the program, the ion optics of four different ion-emitter contours are compared herein. The ion emitter is assumed to be of the porous type, and the effect on the optics of partly blocking the emitter is presented along with focusing, grid size, and grid-spacing effects. A configuration is sought that will yield near-perfect ion optics. Current densities attainable from the various configurations are calculated and discussed.

Lastly, the results of the analysis for the flat ion emitter presented in reference 1 are compared with data obtained from an experimental thruster presently being tested at the NASA Lewis Research Center.

STATEMENT OF PROBLEM AND NUMERICAL SOLUTION

A photograph of the ion thruster from which the mathematical models are established is shown in figure 1. Ions are formed by contact ionization on the porous ion emitter, which is heated and at a positive potential relative to ground. The first grid electrode is usually at a negative potential (except when it is used as a focusing electrode). With an adequate flow of propellant (cesium vapor in this case) assumed, the electric field created between the ion emitter and the first, or accelerator, electrode gives rise to space-charge-limited flow of ions. A net potential difference between the ion emitter and the second, or decelerator, electrode controls the ion-beam exhaust velocity. Shown in figure 2 are a section view of the interior of the thruster (note the region of symmetry and the typical ion trajectory) and a sketch of the idealized potential distribution. It is the solution of the two-dimensional Poisson equation for the region of symmetry shown in figure 2 that is sought.

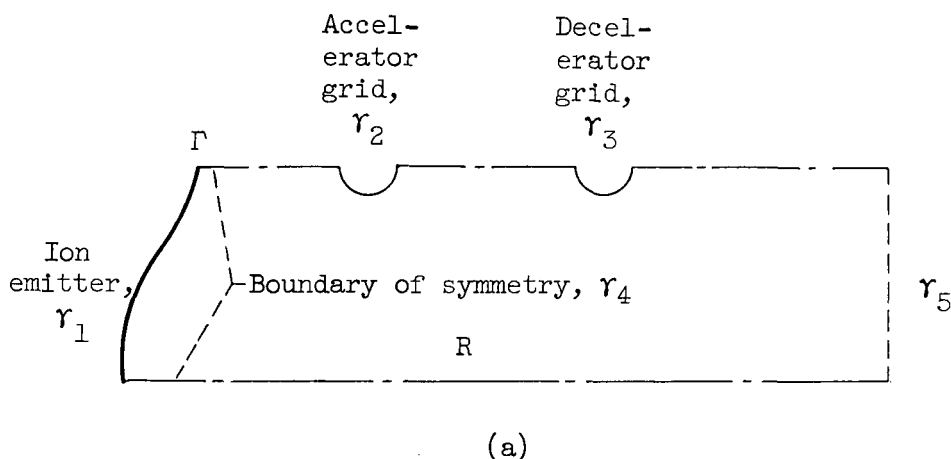
The method of analysis and computer program are given in detail in refer-

ence 1 for the flat ion-emitter configuration. Because of the similarity to the method herein, it will be summarized only up to the point of departure resulting from extending the program to include a contoured ion-emitter boundary.

The method consists of solving numerically the two-dimensional Poisson equation in the form

$$-\nabla^2 \Phi(x,y) = \frac{\rho(\Phi,x,y)}{\epsilon_0} \quad (1)$$

All symbols are defined in the appendix. Equation (1) must be satisfied inside the region R shown in sketch (a). On the boundary Γ of region R, the



equation that applies is

$$\alpha_i \Phi(x,y) + \beta_i \frac{\partial \Phi(x,y)}{\partial n} = \gamma_i \quad \text{for } \alpha \neq \beta; i = 1,2,3,4,5 \quad (2)$$

Two sets of values of α and β were used: 1,0 and 0,1. Values of $\alpha = 1$, $\beta = 0$ represent the Dirichlet boundary condition, and $\alpha = 0$, $\beta = 1$ the Neumann boundary condition.

Equation (1) is solved by numerical techniques by overlaying uniform mesh points (in x,y-coordinates) on the region R. Thus, the continuous equation (eq. (1)) is replaced by a discrete number of equations satisfying the subregions of every mesh point inside the region R. The finite difference approximation of equation (1) for each subregion gives rise to a set of linear algebraic equations. For N mesh points in region R, there are N linear algebraic equations with N unknowns. This set of equations can be expressed in matrix form as

$$A\mathbf{w} = \mathbf{k} \quad (3)$$

where A is the resulting real matrix with positive diagonal and nonpositive off-diagonal entries, \mathbf{w} is the column vector representing the discrete po-

tentials, and \underline{k} is the column vector associated with the external boundary conditions and the space-charge-density function of equation (1). If the column vector \underline{k} is known, equation (3) can be solved by an iterative procedure for the column vector \underline{w} , which is of interest. The column vector \underline{k} in equation (3), however, is not known a priori; and, therefore, a method of overcoming this difficulty must be developed. This problem is discussed later.

The iterative procedure used in reference 1 to solve equation (3) is known as the Cyclic Chebyshev Semi-Iterative method. The selection of this method was based on the properties of the matrix A . For computational convenience, equation (3) is reduced to an analogous matrix equation by premultiplying it by a positive diagonal matrix D such that DA is a matrix with unity on its main diagonal:

$$DA\underline{w} = (I - M)\underline{w} = D\underline{k} \quad (4)$$

The real matrix M is now nonnegative with zero diagonal entries, and it is shown in reference 1 that M is convergent. Equation (4) can be rewritten in the form

$$\underline{w} = M\underline{w} + \underline{g} \quad (5)$$

where $\underline{g} = D\underline{k}$ is again a column vector. By proper numbering of mesh points, the matrix M may be split into two matrices, M_1 and M_2 , such that all odd-number entries depend on even-number entries and vice versa. The Cyclic Chebyshev Semi-Iterative method can now be applied to equation (5) written in the form

$$\left. \begin{aligned} \underline{w}_1^{2m+1} &= \omega_{2m+1} \left(M_2 \underline{w}_2^{2m} + \underline{g}_1 - \underline{w}_1^{2m-1} \right) + \underline{w}_1^{2m-1} & \text{for } m \geq 1 \\ \underline{w}_2^{2m+2} &= \omega_{2m+2} \left(M_1 \underline{w}_1^{2m+1} + \underline{g}_2 - \underline{w}_2^{2m} \right) + \underline{w}_2^{2m} & \text{for } m \geq 0 \end{aligned} \right\} \quad (6)$$

The ω 's are called the relaxation factors, which are given in the form of Chebyshev polynomials. The selection of ω is very important for convergence. For computational purposes, ω is expressed as

$$\omega_{i+1} = \frac{1}{1 - \frac{1}{4} \left[\rho^2(M) \omega_1 \right]} \quad \text{for } i \geq 2$$

$$\omega_1 = 1$$

$$\omega_2 = \frac{2}{2 - \rho^2(M)}$$

where $\rho(M)$ is the spectral radius of the matrix M . Thus, for optimum rate of convergence of equation (6), it is necessary to determine $\rho(M)$. The value of $\rho(M)$ can be calculated by using the so-called "minimax" method, which, for i^{th}

iteration, is written as

$$\min_i \left[\frac{(Mw)_i}{w_i} \right] \leq \rho(M) \leq \max_i \left[\frac{(Mw)_i}{w_i} \right]$$

In order to start the solution of equation (6), it is necessary to supply an initial guess w_2^0 . Although any initial value of w_2^0 would result in convergence, it was found that an initial guess obtained from a semiconducting resistance paper analog saved appreciable computation time.

At this point, all the necessary tools to solve equation (6) are available. As pointed out earlier, though, the column vector k of equation (3) is not known a priori and depends on the potential-distribution function w . Therefore, it is necessary to find some means of overcoming this difficulty. This is done by a method of successive approximations as described in reference 1. First, the potential distribution is calculated with no space charge, that is, solution of the Laplace equation. This potential distribution together with the equations of motion is then used to obtain a first approximation to the space-charge-density function.

The space-charge-density function $\rho(x,y)$ is calculated from the relation

$$\rho(x,y) = \frac{j(x,y)}{v(x,y)}$$

where $j(x,y)$ is the current-density-distribution function and $v(x,y)$ is the velocity-distribution function. Values of $v(x,y)$ are obtained from the relation of conservation of energy. The velocity at the emitter is assumed to be zero. The current-density-distribution function is calculated by dividing the emitter into a large number of equal increments that are bounded by imaginary lines of flow, that is, the ion trajectories. The trajectories that form the boundaries of the "current tubes" are obtained from the equations of motion. By virtue of conservation of charge, the total current flowing through the so-called current tubes remains constant. Because the potential distribution at the first column of mesh points is essentially uniform for the flat ion emitter, the initial direction of the ion trajectories is invariant. This is not the case for the contoured emitter. The current density at the emitter for each tube is approximated from the Child-Langmuir formula for two parallel plates:

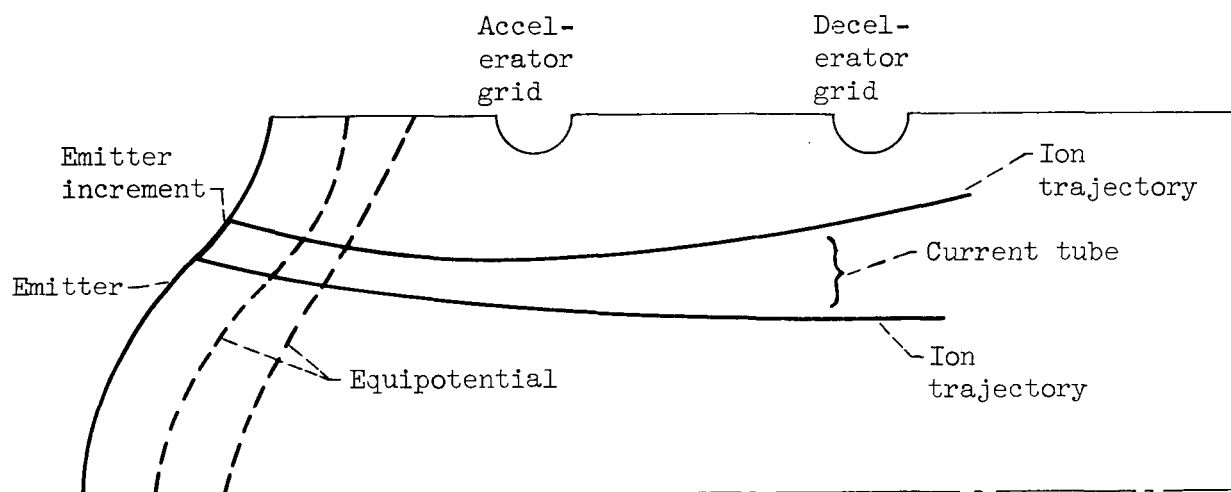
$$j_E = \frac{4}{9} \epsilon_0 \sqrt{\frac{2q}{m}} \frac{\Delta w^{3/2}}{\Delta l^2} \tag{7}$$

Because each mesh point of the first column is located the same distance from the ion emitter in the flat-emitter problem, the length Δl was held constant in equation (7), and the small variations in the discrete potentials at the mesh points of the first column were utilized for the calculation of j_E . As a check on the accuracy of this procedure for the flat ion emitter of reference 1, solutions obtained from the program for a simple flat-plate diode were compared with

known analytic solutions.

In order to obtain solutions for contoured ion-emitter geometries, the previous equations were also applied; however, the computational approach required was somewhat different, and considerable exploration was needed before optimization was accomplished.

Consider a typical test region such as that shown in sketch (b).



(b)

It would be most convenient if equation (7) could be made applicable to the current-density calculation for this geometry. This can be accomplished if the true length of the emitter is calculated, divided into a sufficient number of equal increments, and approximated as a series of straight-line segments. The number of segments chosen would depend on the accuracy desired and, of course, be related to the curvature of the particular geometry under study. The numerical approximations for mesh points occurring along the curved portions of the emitter are calculated by the Mikeladse formula (see ref. 1 for examples). The solution of the Laplacian equation is thus readily obtained. Two differences from the flat-emitter geometry arise in connection with the trajectory and current-density calculations that are necessary for the solution of the Poisson equation. First, the bounding ion trajectories of the current tubes no longer all start in the same direction, so that the initial direction (normal to the emitter) in each trajectory calculation must be taken into account. This accounting presents no particular problem and merely requires addition of the directional information to the program. Second, the equal distance Δl between the emitter and the first mesh column does not exist as before, so that it is no longer convenient to hold Δl constant in equation (7). An alternative is to hold Δw constant, that is, to use the same equipotential line for each current tube and to determine Δl . For this calculation, the equipotential is approximated in each increment as a straight-line segment. The question arises as to what equipotential should be used. At first glance, it would appear natural

for the best accuracy to select an equipotential as close as possible to the emitter to preserve the "parallel-plate" aspect of the equation, if the Child-Langmuir relation is to be used for the current-density approximation. It is to be noted, however, that the current density varies inversely as the square of Δz in equation (7), and small errors in Δz values will be magnified as Δz itself becomes small. Therefore, a point in question is what minimum value of Δz will result in the most accurate numerical solution of equation (6). The problem is further complicated because an optimum suppression factor is not yet known. Suppression factors (SF's) are used to cope with the problem of overestimation of the first approximation of the space-charge-density function obtained from the Laplacian potential distribution and are discussed in detail in reference 1.

To gain some insight into this problem required an investigation of a sample configuration for which the analytic solution is known. The configuration is shown in figure 3 and represents convergent flow between concentric cylinders; this configuration was first analyzed by Langmuir and Blodgett (ref. 2). Convergent-cylindrical space-charge flow is also analyzed for use in an ion thruster configuration in reference 3, where the emitter current density is compared with an equivalent plane diode. The analysis indicates that the emitter current density approximated by an equivalent plane diode (Child-Langmuir formula) would overestimate the current density of convergent-cylindrical flow as the radius ratio of the emitter to the collector departs from unity. As is shown in this analysis, equation (7) is indeed a valid approximation for radius ratios near unity.

Several tests were conducted to determine the minimum distance between the emitter and the equipotential line that would result in optimum potential and current-density distributions. Various dimensions and potentials used for the tests are shown in figure 3 and the results are given in table I, which lists equipotential lines passing through the mesh points 36, 559, 71, and 106 (fig. 3) calculated for a range of SF's. With the exception of an SF of 0.2 for the equipotential through point 36, the potential-distribution deviation from analytic values is less than 3 percent for all equipotential lines. The more significant quantity to compare is the current per unit length (z-direction), which is directly related to the error in distance Δz between the emitter and the equipotential. The deviation of current per unit length for equipotentials very close to the emitter (i.e., less than 2 mesh widths away, through mesh points 36 and 559) varies considerably with SF. It appears important, therefore, when an estimate of the optimum SF is not known to base calculations of j_E on an equipotential that remains at least 3 mesh widths away from the emitter everywhere along the length of the emitter (e.g., equipotential line through point 106). The deviation in current per unit length for the equipotential line through mesh point 106 is less than 10 percent for all SF's.

An estimate of the optimum SF can be obtained as suggested in reference 1. By application of this method it was found that an SF of 0.4, as in reference 1, was close to optimum. Once an estimate of the optimum SF is obtained, the current per unit length can be recalculated by using an equipotential close to the curved emitter boundary. The accuracy of the solution should be improved since the curved segments are being approximated as parallel straight-line segments

(see table I, equipotential line through mesh point 36, $SF = 0.4$). Note that in the calculation of the current per unit length, the current density obtained from equation (7) must be multiplied by a segment length. The length may be the emitter segment length, the equipotential segment length, an average of the two, and so forth. For the sample region, the equipotential segment length yielded better values. The sample region, however, consisted of a completely concave emitter contour. It is probable that for a geometry where the emitter contour contains both concave and convex portions, the segment length should be based on an average value.

To demonstrate the program, solutions were obtained for several example thruster configurations. These results are discussed in the following section.

DISCUSSION OF NUMERICAL EXAMPLES

To demonstrate the use of the numerical-analysis method, a symmetrical module from the ion thruster shown in figure 1 is considered. The region of symmetry is shown in figure 2. Four modular designs with similar electrode configurations but different ion-emitter contours were analyzed. The designs are shown in figure 4, and the coordinates of the ion-emitter contours are given in table II. Module A has a flat ion emitter and represents the experimental thruster configuration shown in figure 1. The compound curve of the ion-emitter contour of module C was determined from a rubber membrane analog as a possible design for lower impingement. The x-coordinates of module B were arbitrarily taken at one-half the value of the module C x-coordinates. The ion-emitter contour of module D is a segment of a circular arc and was selected for study after examining the theoretical predictions from the previous modules. An SF of 0.4 was used throughout the analysis.

Solutions showing the equipotentials and ion trajectories for a net- to acceleration-voltage ratio (hereinafter called net to accel ratio) of 0.5 for the four modules are given in figure 5. A comparison of the Laplace and Poisson potential distributions taken in the plane of the grids and the plane of the centerline is given in table III. The values in these planes represent the extremities of potential that occurred for a given setting. Of particular interest is the "saddle-point" potential in the plane of the centerline. The saddle point is the point of minimum potential in this plane and is of considerable importance with regard to ion thruster operation. Neutralizer electrons injected into the ion beam will be prevented from returning to the thruster provided that the saddle-point potential is sufficiently below that of the electron source. The location of the saddle point was predicted to be approximately the same (1.1 to 1.2 normalized units in the x-direction) for both the Laplace and Poisson solutions and was in approximately the same location for the four contours.

From figure 5 it can be seen that the ion trajectories that constitute the boundary of imaginary current tubes can, in general, (1) pass through the region of the thruster, (2) intersect the grids, (3) cross the plane of $y = 0$, or (4) cross the plane of centerline ($y = 0.5$). For optimum ion thruster performance, it is necessary that all trajectories pass through the region of the thruster unobstructed, so that all the ions formed on the emitter will be utilized for

thrust production. If some of the trajectories strike the grid, the portion of the ion current carried between these trajectories (called the impingement current) is lost. In addition, because of the high energy content of ions hitting the wires, which causes sputtering, the life of the electrode is shortened. Other surface phenomena associated with ion interception are discussed in the following section. The trajectories that cross the boundaries of symmetry are actually not lost in the sense mentioned previously. These trajectories are, however, an indication of beam spreading and reduction of the available thrust. An ideal thruster design would have no impingement current and a well collimated ion beam.

From figure 6, which shows the theoretical percent impingement current as a function of net to accel ratio for the four modular designs, it can be seen that a contoured ion emitter is one way to reduce ion impingement current. Unfortunately, of the four contours analyzed, none meets the requirement of near-perfect optics. For that reason, some other means of reducing the impingement current were investigated.

One improved design was the blockage of that area of the ion emitter that had contributed a major portion of the impingement current. A limiting trajectory was chosen that divided the region of no space charge and the region of ion flow. The effect is shown in figure 7 for contours C and D for two net to accel ratios, 0.5 and 0.2. Decreasing this ratio (i.e., increasing the current density) gives rise to greater beam spreading, which is consistent with the electron-optics phenomena discussed in reference 4. The design of a partly blocked ion-emitter surface proved to be effective in reducing the theoretically predicted impingement current to zero for contour D.

Another method often used experimentally to eliminate impingement current is the use of a focusing electrode. In this analysis, focusing was achieved by applying the same potential to the first grid and ion emitter and by using the second grid as an accelerator. The theoretical result of applying this technique to contour C with a partly blocked ion-emitter surface is shown in figure 8 for two different grid spacings. The effect of spacing between the ion emitter and the focusing electrode on the ion trajectories shows an increase in beam spreading with decreasing spacing. Impingement is reduced to zero. The use of a focusing electrode was found very promising and was also applied to the flat ion emitter, module A. The result is shown in figure 9 for two grid spacings. The reduction in predicted impingement current from the values given in figure 6 for the flat emitter, module A, is striking. Contrary to the results for the previous configuration (fig. 8), decreasing the spacing between the emitter and the focusing electrode appears to reduce the beam spreading.

The effect of reducing the grid-wire diameter was next investigated for module A with a focusing electrode. The results are shown in figure 10 and can also be compared with those of figure 9(b). The average current density increased as the wire diameter was reduced, while the total percent impingement current decreased slightly.

Thus far, the discussion presented in this section has been oriented toward the reduction of ion impingement current. No reference has been made to the

effect on the ion-emitter current density of all the methods used to minimize impingement. Attention is now directed to this area. Average current densities for the initial four modules analyzed are shown in figure 11 for a range of net to accel ratios. The values shown are the average space-charge-limited current densities for 1 millimeter spacing between the emitter and the accelerator grid, for the configurations shown in figure 4. A comparison with the ideal current density from the Child-Langmuir formula for a plane diode is included. It is apparent that the current densities for the four modules follow quite closely the $3/2$ power of Child's law. The average current density for the modules was obtained as a sum of the total currents flowing through the tubes divided by the length of the emitter (length in z-direction is taken as unity):

$$\bar{J} = \frac{\sum_{k=1}^n \left[j_E(\delta l)_E \right]_k}{l_E}$$

where $(\delta l)_E$ is the emitter segment length between trajectories. The current density is not constant across the emitter, as can be surmised from figure 5. The current-density distribution across the emitter in the y-direction is shown in figure 12 for module D, where all physical dimensions are in millimeters. It is interesting to note that the local current density for any tube is higher for the partly blocked ion-emitter surface than for the unblocked emitter. This difference explains why the average current density of the partly blocked emitter is not merely equal to the average current density for the unblocked emitter multiplied by the percent of effective area. For example, for module D, the average current density for a net to accel ratio of 0.5 is 239.48 amperes per square meter. For the same voltages for the partly blocked ion emitter, the average current density is 205.95 amperes per square meter or 86 percent of the unblocked emitter. On the other hand, the ion-emitter area for the partly blocked emitter was 80 percent of the unblocked emitter area. A change in the relative positions of the equipotentials for these two examples (see figs. 5(d) and 7(c)) accounts for this difference. The difference is even more pronounced at lower net to accel ratios. Thus, although the average current density is not lowered in direct proportion to the blocked emitter area, the lower average current density nevertheless does result in a lower thrust per unit area and possibly in a lower overall power efficiency.

The average current densities obtained with the focusing-accelerator arrangement are given in figures 8 to 10. The low values (compared with values from the accelerator-decelerator arrangement) are primarily a result of the increased spacing between the emitter and the accelerator grid.

In order to evaluate the relative merits for a given configuration that would incorporate both the effect of power loss due to impingement current and current density, beam power per unit length (in the z-direction) at the exit is plotted in figure 13 (see table IV also) against grid power efficiency for all configurations examined. The grid power efficiency is defined as

$$\eta_G = \frac{P_B}{P_B + P_G}$$

where P_G is the sum of the grid impingement current times the voltage difference between the ion emitter and the respective grids. The grid power efficiency can be expressed as

$$\eta_G = \frac{(J_{ex}/J_E)(\phi_{net}/\phi_{accel})}{(J_{ex}/J_E)(\phi_{net}/\phi_{accel}) + J_{accel}/J_E + (J_{decel}/J_E)(\phi_{net}/\phi_{accel})}$$

This plot, then, except for the effect of beam spreading, gives a comparative evaluation of all configurations tested. It is apparent that module D with a partly blocked ion emitter (points 40 and 41 in fig. 13) gives the best grid performance based on this comparison, that is, maximum grid power efficiency and current density. The flat emitter, module A, with focusing also gives good results (points 10 to 13 in fig. 13).

To compute the engine power efficiency, as defined in reference 3, requires accounting for the power losses incurred because of beam spreading. For points 40 and 41, for example, this loss was estimated from trajectory plots to be less than 2.0 percent.

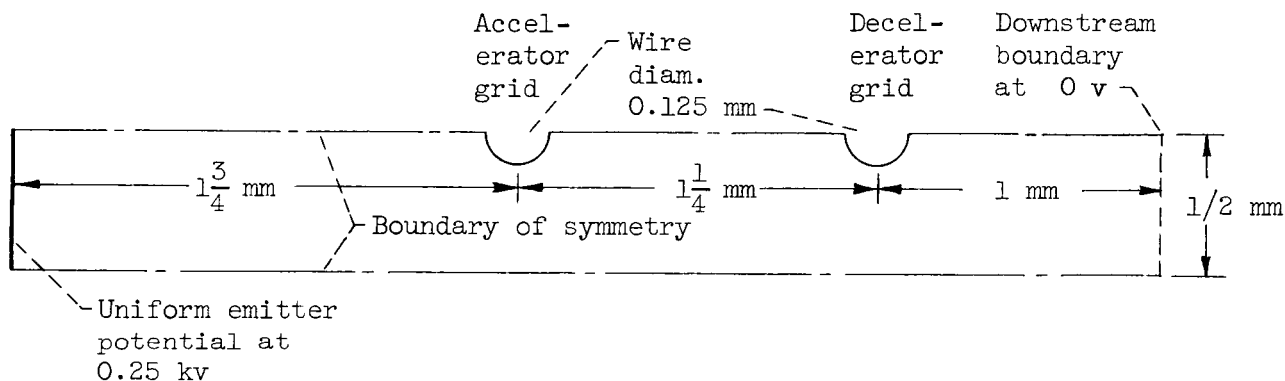
COMPARISON OF ANALYTICAL WITH EXPERIMENTAL RESULTS

As mentioned previously, the mathematical models were chosen to be typically representative of an experimental ion thruster presently being tested at the NASA Lewis Research Center (fig. 1). An experiment was conducted in which the thruster array was similar to module A. Electrical circuitry used for obtaining desired potential settings and for measuring the ion-emitter and intercepted currents is shown schematically in figure 2. The experiment was conducted in a 1.07-meter-diameter by 2.14-meter-long stainless-steel vacuum facility. Experimental procedures and techniques used in this test were similar to those reported in reference 5.

In this test, the flat ion emitter was of the porous-tungsten contact-ionization type. The emitter surface (13.9 sq cm) was heated from behind by thermal radiation from a resistance-heated strip of tungsten. There were 126 tantalum wires (0.125 mm diam.) spaced 1 millimeter apart in each grid. The spacing of grids (in the x-direction) was $1\frac{3}{4}$ millimeters between the emitter and the accelerator grid and $1\frac{1}{4}$ millimeters between the accelerator and the decelerator grids. The emitter and the decelerator-grid potentials were kept constant at 0.25 and 0 kilovolt, respectively, for the duration of the test. The accelerator-grid potential was varied to cover a range of net to accel ratios. A neutralizer wire was located downstream about 43 centimeters from the exit of the thruster. The wire was kept at a potential of 0 and was resistance heated

to a constant temperature for the duration of the test. The cesium vaporizer temperature was maintained constant at about 660 K. Ion-emitter, accelerator- and decelerator-grid currents were monitored by conventional multirange meters. Data were taken by varying the accelerator voltage in 50-volt steps at 1- to 2-minute intervals.

The mathematical model that was analyzed and compared with the previously mentioned experiment is shown in sketch (c).



(c)

A comparison of experimental and analytical percent impingement current is shown in figure 14 for a range of net to accel ratios. Values are expressed as a percent of the ion-emitter current. Good agreement for the low range (less than 0.5) of net to accel ratios was obtained: at higher ratios, agreement was poor. Several real effects that are not included in the theoretical analysis may arise in the experimental investigation. The order of magnitude of some of these effects is considered in the discussion that follows.

Although the experiment was conducted at a constant propellant flow rate, conditions of the test were such that the emitter current varied from space-charge limited to vaporizer-temperature limited. Therefore, not all of the cesium vapor passing through the porous-tungsten emitter was ionized. From the ratio of emitter current to total propellant flow rate, the neutral efflux was estimated to vary between 20 and 60 percent over the low range (less than 0.5) of net to accel ratios. The presence of these neutral particles together with the charged particles gives rise to the possible occurrence of charge exchange. This problem is discussed in reference 6. Estimates made by using the relations developed in reference 6 indicate that, for the range of test conditions, the ratio of charge exchange current density to the average emitter current density would be much less than 1 percent.

The grid wires were at a high temperature (1000° K) because of the close spacing of the grids with respect to the emitter, whose surface was maintained at about 1470° K. The temperature of the grids, together with the existence of electric fields between the emitter and the accelerator and decelerator grids, could result in several phenomena that may be grouped under the heading of

surface processes.

The arrival of neutral atoms at the hot surfaces of the grid wires could produce thermionic emission. For every electron emitted from the grid wires by this process, there must be a new one supplied from ground. This would be registered on the meter that monitors the grid impingement current and cause the meter to indicate a larger current than that due to ion impingement alone. It was estimated from reference 7 that a correction accounting for this effect, if applied to the accelerator grid meter could result in a lowering of the ratio of accelerator-grid impingement to emitter current by 1.0 to 13.0 percent (average 7 percent) over the range of net to accel ratios less than 0.5. Since the decelerator grid is shadow shielded from the ion emitter by the accelerator grid and is at a lower temperature, it is unlikely that the decelerator grid would contribute to this phenomenon.

The presence of electric fields could produce field emission; however, the highest value of such a field was estimated from the analysis to be about 5×10^4 volts per centimeter and, according to reference 8, is not large enough to cause any significant electron current flow by this means.

Another effect that may give rise to electron emission from the grids without being isolated by the metering system is emission of electrons as a result of high-energy ions striking the surface. For the test considered, the ions were of low energy (1 kv or less), and from available yield coefficients for cesium ions (ref. 9), it was estimated that, due to this effect, the measured ratio of accelerator-grid impingement to emitter current could have been too large by about 2.5 percent.

All effects discussed thus far would be predominantly associated with the accelerator grid and would tend to cause an "apparent" intercepted current greater than that due to ion impingement alone. The total magnitude of these effects for net to accel ratios less than 0.5 was estimated to be of the order of 10 percent. Thus, although figure 14 indicates experimental values of about 21 percent accelerator-grid impingement, the values could be 10 percent lower. The analytical values of about 15 to 16 percent over this range therefore seem reasonable.

The effect of electron arrival at the grids and the emitter from the neutralizer wire was estimated as most significant, in particular for the high net to accel ratios. As these ratios increased from 0.5 to 1.0, the analysis indicates that the saddle-point potential increased from -125 volts to a value above ground. In this event it could be assumed that electrons from the neutralizer would be permitted to travel upstream and to enter the thruster. The meter that indicates the emitter current would then show higher values than those resulting from ion production alone. The meters that indicate electron flow to the grids (because of ion interception) may show lower readings as a result of possible arrival of the neutralizer electrons at the grids. This is the most likely explanation for a discrepancy between the analytical and the experimental impingement currents for net to accel ratios greater than 0.5. Even for the lower ratios (fig. 14), the low impingement measured on the decelerator grid might be attributed to this effect.

The experimental ion-emitter current is shown in figure 15. Values are compared with the results of the numerical analysis and the theoretically predicted values for a plane triode (from ref. 10). The departure of experimental values from the analytic curve for net to accel ratios greater than 0.5 is most probably due to the arrival of electrons from the neutralizer wire, whereas for the lower ratios (less than 0.3) the deviation is most probably due to the limited cesium flow rate.

As a final comparison, experimental results reported in reference 11, for a geometry similar to that shown in figure 10(a), indicate ion-impingement current of 0.2 percent. Unfortunately, no applied voltages are mentioned in reference 11, and a comparison with the theoretical prediction of 0.72 percent given in figure 10(a) can only be qualitative. Figure 6 shows that, for a given configuration, the total percent impingement current is almost constant over a range of net to accel ratios. If this indication is valid, the experimental results reported in reference 11 and the result obtained by this analysis show good quantitative agreement.

CONCLUDING REMARKS

The numerical solution of the two-dimensional Poisson equation has been successfully generalized to include contoured ion emitters. The accuracy of the solution was compared with a sample model of a convergent-cylindrical diode whose analytic solution is known. Potential distributions were found to agree within 3 percent for all cases tested except one. The use of an optimum suppression factor resulted in values of current per unit length that agreed within 3 percent.

The numerical method was used to evaluate the ion optics and thus the performance of several ion-thruster configurations with closely spaced grids. Perfect optics in the sense of zero impingement was achieved in several cases by applying the following geometric modifications:

- (1) Partly blocking the ion emitter surface
- (2) Using focusing techniques
- (3) Both (1) and (2) together with appropriate spacing and size of the grids.

Results showed that a partly blocked ion emitter caused the ion-emitter current density to be reduced by values that were less than in direct proportion to the reduction in emitter area. Comparison of all configurations analyzed showed that a partly blocked circular-arc ion emitter produced the highest beam power with zero impingement. The flat emitter with a focusing electrode was shown to be quite good also and may be a more attractive design from the viewpoint of ease of fabrication.

From the test results obtained with a Lewis thruster similar in design to the flat-emitter model, the percent current impingement for net- to acceleration

voltage ratios less than 0.5 shows good agreement. Similarly, total ion-emitter current compares very well over this range. For higher net- to acceleration-voltage ratios, the backstreaming of electrons from the neutralizer prevented accurate measurement of ion-impingement current. Impingement currents reported by another investigator (ref. 11) for a configuration similar to the flat-emitter model and incorporating a focusing electrode also agree quite well with the analysis herein.

The application of numerical analysis to the space-charge flow in an ion thruster has been demonstrated, and it would be possible to use the method to check the ion optics for essentially any specified ion-accelerator geometry for which the two-dimensional analysis would be adequate.

Lewis Research Center

National Aeronautics and Space Administration

Cleveland, Ohio, January 28, 1963

APPENDIX - SYMBOLS

A	matrix of matrix equation (eq. (3)), area, sq m
D	matrix, multiplier of matrix A
$g_{1,2}$	column vectors, odd and even, respectively
\underline{g}	column vector, \underline{Dk}
I	unit matrix
J	current, amp
j	current density, amp/sq m
\bar{j}	average current density, amp/sq m
\underline{k}	column vector of matrix equation (eq. (3))
l	length of emitter, or distance between emitter and equipotential, m or mm
M	real matrix with zero diagonal entries
$M_{1,2}$	matrix consisting of odd and even entries of M, respectively
m	particle mass, kg
n	outward normal
P	power, w
q	unit charge, coulombs
R	region
r	radius of test region in fig. 3 and table I
v	velocity, m/sec
w	potential-distribution function for discrete case, kv or component of vector \underline{w}
\underline{w}	column vector of matrix equation (eq. (3))
$\underline{w}_{1,2}$	column vectors, odd and even, respectively
x,y	Cartesian coordinates
α, β	integers (1 or 0)

Γ	external boundary of R
r	discrete portion of external boundary
Δ	increment
∇^2	Laplacian operator
δl	segment length between trajectories
ϵ_0	permittivity of free space, coulombs/(v)(m)
η	efficiency
ρ	space-charge-density-distribution function, coulombs/cu m
$\rho(M)$	spectral radius of matrix M
Φ	potential-distribution function for continuous case, kv
ω	relaxation factor

Subscripts:

accel	accelerator grid, or as defined in fig. 2
B	beam
decel	decelerator grid
E	emitter
ex	exit
G	grid
i	number, 1, 2, . . . , N
k	number, 1, 2, . . . , n
m	number of iteration
N	number of mesh points
n	number of ion trajectory
net	defined in fig. 2
x,y	direction

Superscripts:

m number of iteration

o initial guess

REFERENCES

1. Hamza, Vladimir, and Richley, Edward A.: Numerical Solution of Two-Dimensional Poisson Equation: Theory and Application to Electrostatic-Ion-Engine Analysis. NASA TN D-1323, 1962.
2. Langmuir, I., and Blodgett, K.: Currents Limited by Space Charge Between Coaxial Cylinders. Phys. Rev., ser. 2, vol. 22, no. 4, Oct. 1923, pp. 347-356.
3. Lockwood, D. L., Mickelsen, W. R., and Hamza, V.: Analytic Space-Charge Flow and Theoretical Electrostatic Rocket Engine Performance. Paper 2400-62, Am. Rocket Soc., Inc., 1962.
4. Dolder, K. T., and Klemperer, O.: Space-Charge Effects in Electron Optical Systems. Jour. Appl. Phys., vol. 26, no. 12, Dec. 1955, pp. 1461-1471.
5. Lockwood, David L., and Cybulski, Ronald J.: Performance Evaluation of a Two-Dimensional Ion Rocket Using Through-Feed and Porous Tungsten Ionizers. NASA TN D-766, 1961.
6. Reynolds, Thaine W., and Childs, J. Howard: A Comparison of Reverse-Feed and Porous-Tungsten Ion Engines. NASA TN D-1166, 1962.
7. Gibbons, M. D.: Investigation of Emission from Electrode Systems in Cesium Vapor. Sci. Rep. 9, AFCL 400, Air Res. and Dev. Command, USAF, Mar. 1961.
8. Francis, Gordon: Ionization Phenomena in Gases. Butterworths Sci. Pub., 1960.
9. Kuskevics, G., Speiser, R. C., Worlock, R. M., and Zuccaro, D.: Ionization, Emission, and Collision Processes in the Cesium Ion Engine. Paper 2364-62, Am. Rocket Soc., Inc., 1962.
10. Spangenberg, K. R.: Vacuum Tubes. McGraw-Hill Book Co., Inc., 1948, p. 186.
11. Shelton, Haywood: Experiments on Atom and Ion Emission from Porous Tungsten. Paper 2360-62, Am. Rocket Soc., Inc., 1962.

TABLE I. - NORMALIZED DATA FOR TEST REGION SHOWN IN FIGURE 3

(a) Equipotential line through mesh point 36.

Test-region point, radius, r	Mesh point, N	Continuous potential, ϕ	Suppression factor										
			Execution time, min										
			0.2	0.3	0.4	0.5	0.6	0.7	0.8				
			4.0	3.4	5.1	4.4	4.7	4.9	6.0				
			Current per unit length of emitter, J/l , amp/mm										
			2.396 $\times 10^{-2}$	0.7428 $\times 10^{-2}$	0.7575 $\times 10^{-2}$	0.9294 $\times 10^{-2}$	1.186 $\times 10^{-2}$	1.151 $\times 10^{-2}$	1.123 $\times 10^{-2}$				
			Percent deviation of current per unit length of emitter										
			226.0	1.00	2.99	26.37	61.30	56.54	52.68				
1.15 1.10 1.05 1.00 .95 351 90 85 80 75 70 65	71 141 211 281 351 421 491 561 631 701 771	0.9732 .9331 .8796 .8207 .7471 .6713 .5876 .4940 .3885 .2465 .1417	Discrete potential, w	Discrete potential, w	Deviation, percent	Discrete potential, w	Deviation, percent	Discrete potential, w	Deviation, percent	Discrete potential, w	Deviation, percent		
			0.9538	0.9733	-0.22	0.9710	0.23	0.9709	0.24	0.9682	0.51	0.9691	0.42
			.9004	.9356	-0.27	.9292	.42	.9286	.48	.9242	.95	.9254	.82
			.8410	.8854	-0.66	.8781	.17	.8768	.32	.8712	.95	.8726	.80
			.7758	.8251	-0.86	.8185	.27	.8165	.51	.8102	1.28	.8116	1.11
			.7048	.7579	-1.44	.7505	-0.42	.7480	-1.12	.7413	1.78	.7426	.60
			.6275	.6810	-1.44	.6741	-0.42	.6712	.01	.6644	1.03	.6656	.85
			.5438	.5949	-1.24	.5888	-0.20	.5856	.34	.5791	1.11	.5802	1.26
			.4528	.4932	-1.05	.4839	.02	.4808	.65	.4850	1.82	.4858	1.66
			.3540	.3930	-1.16	.3868	-0.08	.3811	.84	.3811	1.90	.3817	1.75
			.2696	.2753	-2.11	.2724	-1.04	.2702	-0.22	.2665	1.15	.2670	.2874
			.1417	.1493	-2.26	.1433	-1.13	.1420	-0.21	.1400	1.20	.1403	.199

(b) Equipotential line through mesh point 559.

Test-region radius, r	Mesh point, N	Contin-uous po-tential, ϕ	Suppression factor											
			Execution time, min											
			0.2	0.3	0.4	0.5	0.6	0.7	0.8					
	4.1		4.0		4.3		5.5		3.7		4.4		5.7	
Current per unit length of emitter, J/l , amp/mm														
			0.9539 $\times 10^{-2}$		0.8888 $\times 10^{-2}$		0.8921 $\times 10^{-2}$		0.8851 $\times 10^{-2}$		0.8539 $\times 10^{-2}$		0.8558 $\times 10^{-2}$	
Percent deviation of current per unit length of emitter														
	29.70		20.85		21.29		20.35		16.09		13.66		16.36	
	Discrete potential, w	Devia-tion, percent	Discrete potential, w	Devia-tion, percent	Discrete potential, w	Devia-tion, percent	Discrete potential, w	Devia-tion, percent	Discrete potential, w	Devia-tion, percent	Discrete potential, w	Devia-tion, percent	Discrete potential, w	
1.15	0.9732	0.9710	0.9724	0.08	0.9722	0.10	0.9724	0.08	0.9731	0.01	0.9735	-0.03	0.9733	
1.10	.9331	.9290	.9305	.28	.9302	.31	.9309	.24	.9316	.16	.9324	.08	.9323	
1.05	.8796	.8774	.8787	.10	.8784	.14	.8796	0.	.8802	-.07	.8812	-.18	.8813	
1.00	.8207	.8174	.8183	.29	.8180	.33	.8195	.15	.8200	.08	.8211	-.05	.8214	
.95	.7471	.7491	.7496	-.33	.7493	-.29	.7510	-.32	.7513	-.56	.7525	-.72	.7531	
.90	.6713	.6724	.6725	-.18	.6722	-.13	.6741	-.42	.6742	-.43	.6754	-.61	.6761	
.85	.5876	.5869	.5867	.15	.5864	.20	.5882	-.12	.5883	-.12	.5894	-.31	.5902	
.80	.4940	.4922	.4917	.47	.4914	.53	.4932	.16	.4931	.18	.4941	-.02	.4950	
.75	.3885	.3873	.3866	.49	.3865	.51	.3880	.13	.3878	.18	.3887	-.05	.3895	
.70	.2696	.2712	.2706	-.36	.2705	-.33	.2718	.70	.2715	-.70	.2721	-.93	.2728	
.65	.1417	.1427	.1423	-.42	.1422	-.35	.1429	-.85	.1428	-.78	.1431	-.99	.1435	

(c) Equipotential line through mesh point 71.

Test-region radius, r	Mesh point, N	Contin- uous po- tential, ϕ	Suppression factor									
			0.2	0.3	0.4	0.5	0.6	0.7	0.8			
Execution time, min												
	3.9		3.6		3.5		3.4		4.5		4.5	5.2
Current per unit length of emitter, J/l , amp/mm												
	0.8442×10^{-2}		0.8039×10^{-2}		0.8147×10^{-2}		0.8365×10^{-2}		0.8317×10^{-2}		0.8273×10^{-2}	0.8280×10^{-2}
Percent deviation of current per unit length of emitter												
	14.78		9.30		10.77		13.74		13.09		12.48	12.59
	Discrete potential, w	Devia- tion, percent	Discrete potential, w	Devia- tion, percent	Discrete potential, w	Devia- tion, percent	Discrete potential, w	Devia- tion, percent	Discrete potential, w	Devia- tion, percent	Discrete potential, w	Devia- tion, percent
1.15	71	0.9732	0.9722	0.10	0.9738	-0.06	0.9734	-0.21	0.9728	0.04	0.9728	0.04
1.10	141	.9331	.9311	.21	.9331	0.	.9323	.09	.9315	.17	.9313	.19
1.05	211	.8796	.8801	.05	.8823	-.31	.8812	-.18	.8804	-.09	.8799	-.03
1.00	281	.8207	.8205	.02	.8226	-.23	.8212	-.06	.8205	.02	.8197	.12
.95	351	.7471	.7524	-.71	.7542	-.95	.7526	-.58	.7522	-.68	.7511	-.54
.90	421	.6713	.6758	-.67	.6773	-.89	.6755	-.63	.6753	-.60	.6740	-.40
.85	491	.5876	.5902	-.44	.5914	-.65	.5896	-.34	.5895	-.32	.5882	-.10
.80	561	.4940	.4951	-.22	.4960	-.40	.4943	-.06	.4944	-.08	.4930	.20
.75	631	.3885	.3898	-.33	.3905	-.46	.3888	-.08	.3890	-.13	.3878	.18
.70	701	.2696	.2731	-1.30	.2733	-1.40	.2722	-.96	.2724	-1.04	.2715	-.70
.65	771	.1417	.1437	-1.41	.1438	-1.50	.1432	-1.06	.1433	-1.13	.1428	-.78

(d) Equipotential line through mesh point 106.

Test-region radius, r	Mesh point, N	Continuous potential, ϕ	Suppression factor													
			Execution time, min						Current per unit length of emitter, J/l , amp/mm							
			0.2		0.3		0.4		0.5		0.6		0.7		0.8	
			3.9		4.2		4.0		3.5		3.4		3.8		5.4	
			Percent deviation of current per unit length of emitter													
			0.8017x10 ⁻²		0.8033x10 ⁻²		0.8038x10 ⁻²		0.8041x10 ⁻²		0.8038x10 ⁻²		0.8041x10 ⁻²		0.8040x10 ⁻²	
			9.00		9.21		9.29		9.33		9.28		9.33		9.32	
			Discrete potential, w	Deviation, percent	Discrete potential, w	Deviation, percent	Discrete potential, w	Deviation, percent	Discrete potential, w	Deviation, percent	Discrete potential, w	Deviation, percent	Discrete potential, w	Deviation, percent	Discrete potential, w	Deviation, percent
1.15	71	0.9732	0.9727	0.05	0.9729	0.03	0.9728	0.04	0.9728	0.04	0.9728	0.04	0.9728	0.04	0.9728	0.04
1.10	141	.9331	.9319	.13	.9314	.18	.9314	.18	.9314	.18	.9314	.18	.9314	.18	.9314	.18
1.05	211	.8796	.8813	-.13	.8801	-.06	.8800	-.04	.8801	-.06	.8801	-.06	.8800	-.04	.8800	-.04
1.00	281	.8207	.8218	-.13	.8199	-.10	.8198	.11	.8199	.10	.8200	.09	.8199	.10	.8198	.11
.95	351	.7471	.7538	-.90	.7514	-.58	.7512	-.55	.7512	-.55	.7514	-.58	.7512	-.55	.7512	-.55
.90	421	.6713	.6772	-.88	.6744	-.46	.6741	-.42	.6742	-.43	.6743	-.45	.6742	-.43	.6741	-.42
.85	491	.5876	.5916	-.68	.5866	-.17	.5863	-.12	.5865	-.12	.5865	-.15	.5863	-.12	.5862	-.10
.80	561	.4940	.4964	-.49	.4934	.12	.4931	.18	.4931	.18	.4933	.14	.4931	.18	.4930	.20
.75	631	.3885	.3908	-.59	.3882	.08	.3878	.18	.3878	.18	.3881	.10	.3878	.18	.3878	.18
.70	701	.2696	.2739	-1.59	.2718	-.82	.2715	-.70	.2715	-.70	.2717	-.78	.2715	-.70	.2715	-.70
.65	771	.1417	.1442	-1.76	.1430	-.92	.1428	-.78	.1428	-.78	.1429	-.85	.1428	-.78	.1428	-.78

TABLE II. - NORMALIZED ION-EMITTER

COORDINATES FOR MODULES SHOWN

IN FIGURE 4

[Modules symmetrical about centerline.]

y	Module			
	A	B	C	D
	x			
0	0	0	0	0.056
.05	↓	-.002	-.005	0
.10		-.011	-.022	-.045
.15		-.025	-.050	-.082
.20		-.046	-.092	-.112
.25		-.062	-.125	-.138
.30		-.075	-.150	-.156
.35		-.084	-.167	-.171
.40		-.090	-.180	-.180
.45		-.094	-.188	-.188
.50		-.095	-.190	-.190

TABLE III. - LAPLACIAN AND POISSON POTENTIAL DISTRIBUTIONS FOR
MODULE CONFIGURATIONS SHOWN IN FIGURE 4

[Net- to acceleration-voltage ratio, 0.5; units, kilovolts.]

Normal- ized dis- tance, x	Module							
	A		B		C		D	
	Laplacian	Poisson	Laplacian	Poisson	Laplacian	Poisson	Laplacian	Poisson
Plane of grids								
0.	1.000	1.000	1.000	1.000	1.000	1.000	-----	-----
.056	.903	.961	.884	.954	.868	.948	1.000	1.000
.2	.661	.808	.621	.784	.592	.766	.597	.751
.4	.319	.519	.280	.490	.253	.468	.254	.446
.6	-.039	.157	-.067	.134	-.087	.115	-.087	.094
.8	-.467	-.334	-.480	-.346	-.491	-.358	-.491	-.370
1.0	-1.000	-1.000	-1.000	-1.000	-1.000	-1.000	-1.000	-1.000
1.2	-.662	-.546	-.660	-.544	-.663	-.549	-.663	-.557
1.4	-.460	-.291	-.456	-.286	-.458	-.292	-.458	-.307
1.6	-.316	-.147	-.311	-.141	-.312	-.147	-.313	-.160
1.8	-.166	-.051	-.163	-.046	-.164	-.049	-.164	-.055
2.0	0	0	0	0	0	0	0	0
2.2	-.043	.044	-.040	.054	-.040	.054	-.040	.063
2.4	-.045	.073	-.042	.086	-.042	.086	-.042	.101
2.6	-.033	.075	-.031	.085	-.031	.087	-.031	.106
2.8	-.017	.050	-.016	.056	-.016	.058	-.016	.072
3.0	0	0	0	0	0	0	0	0
Plane of centerline								
-0.190	-----	-----	-----	-----	1.000	1.000	1.000	1.000
-.095	-----	-----	1.000	1.000	.911	.968	.909	.969
0	1.000	1.000	.877	.950	.806	.912	.802	.911
.2	.666	.813	.591	.761	.545	.731	.541	.728
.4	.336	.540	.287	.505	.255	.484	.253	.482
.6	.021	.234	-.010	.215	-.033	.204	-.034	.205
.8	-.251	-.055	-.543	-.059	-.283	-.059	-.283	-.055
1.0	-.424	-.247	-.431	-.237	-.440	-.232	-.440	-.220
1.2	-.464	-.290	-.464	-.271	-.469	-.263	-.469	-.241
1.4	-.409	-.233	-.405	-.208	-.408	-.199	-.409	-.171
1.6	-.315	-.144	-.310	-.116	-.312	-.106	-.312	-.074
1.8	-.217	-.061	-.212	-.032	-.213	-.022	-.213	.012
2.0	-.138	.007	-.133	.033	-.133	.042	-.133	.081
2.2	-.087	.059	-.083	.079	-.083	.086	-.084	.130
2.4	-.057	.090	-.054	.103	-.054	.107	-.055	.151
2.6	-.036	.093	-.034	.102	-.034	.103	-.034	.143
2.8	-.018	.062	-.017	.070	-.017	.072	-.017	.095
3.0	0	0	0	0	0	0	0	0

TABLE IV. - SUMMARY OF ALL CONFIGURATIONS ANALYZED BY THE NUMERICAL METHOD OF THIS REPORT (SEE FIG. 13)

Fig- ure 13 data point number	Module	Emitter length, mm	Wire diam- eter, mm	Exit length, mm	Potential		Average current density, amp/sq m	Impingement current, percent				Beam power unit length, w/m	Grid power effi- ciency, percent	Spacing between	
					ϕ_{net} , kv	ϕ_{accel} , kv		Focus- ing grid	Accel- erator grid	Decel- erator grid	Total			Emitt- er and first grid, mm	First and second grid, mm
1	A	0.5000	0.125	0.4375	1.0	1.0	138.3	---	18.30	15.08	33.38	44.41	66.62	1	1
2					1.25	1.25	179.3	---	18.78	13.53	32.31	60.68	64.66	1	1
3					1.67	1.67	265.3	---	19.28	11.29	30.57	92.12	61.49	1	1
4					2.0	2.0	341.8	---	19.57	10.95	30.52	118.74	58.11	1	1
5					2.5	2.5	467.4	---	19.97	9.85	29.82	164.05	54.01	1	1
6					5.0	5.0	1266.0	---	20.81	7.00	27.81	457.01	39.40	1	1
7					1.0	1.0	5.88	2.05	2.97	---	5.02	2.85	98.5	1/2	1
8					2.0	2.0	14.93	4.56	3.10	---	7.66	7.23	93.97	1	1
9					1.0	1.0	22.40	2.56	.890	---	3.45	10.82	99.09	1	1
10					2.0	2.0	58.36	2.56	1.00	---	3.56	28.14	97.98	1	1
11					2.0	2.0	72.31	.72	0	---	.72	36.15	100.0	1	1
12					1.0	1.0	35.98	.84	0	---	.84	17.84	100.0	1	1
13					2.0	2.0	76.60	.64	0	---	.64	38.07	100.0	1	1
14	B	0.5160	0.125	0.4375	1.0	1.0	122.0	---	13.36	12.38	25.74	48.67	75.03	1	1
15					1.25	1.25	164.0	---	13.68	10.56	24.24	64.09	73.24	1	1
16					1.67	1.67	242.8	---	14.03	8.97	23.00	96.41	70.38	1	1
17					2.0	2.0	312.5	---	14.16	8.07	22.23	125.4	68.12	1	1
18					2.5	2.5	431.7	---	14.27	7.48	21.75	174.3	64.44	1	1
19					5.0	5.0	1175.0	---	14.63	8.02	22.65	468.9	48.79	1	1
20					1.0	1.0	101.2	---	11.87	10.23	22.10	43.54	77.90	1	1
21	C	0.5520	0.125	0.4375	1.0	1.0	136.1	---	12.27	8.96	21.23	59.19	76.42	1	1
22					1.25	1.25	201.5	---	12.71	8.13	20.84	88.06	72.96	1	1
23					1.67	1.67	259.4	---	12.92	7.70	20.62	113.7	70.30	1	1
24					2.0	2.0	358.3	---	13.02	7.48	20.50	157.3	66.52	1	1
25					2.5	2.5	975.7	---	13.37	6.52	19.89	431.6	52.20	1	1
26					5.0	5.0	93.62	---	5.09	0	5.09	39.26	94.89	1	1
27					1.0	1.0	239.9	---	13.15	0	13.15	92.06	76.76	1	1
28					2.0	2.0	900.5	---	7.72	0	7.72	367.17	70.50	1	1
29					5.0	5.0	10.45	8	0	---	0	4.62	100.0	1/2	1
30					2.0	2.0	29.13	0	0	---	0	12.87	100.0	1	1
31					1.0	1.0	9.07	2.53	0	---	2.53	4.88	100.0	1	1
32					1.0	1.0	12.50	2.15	1.17	---	3.32	6.67	98.80	1/2	1
33					2.0	2.0	32.53	2.15	1.26	---	3.41	17.35	97.46	1/2	1
34	D	0.5770	0.125	0.4375	1.0	1.0	88.92	---	4.02	5.46	9.48	46.45	90.52	1	1
35					1.25	1.25	119.5	---	4.08	7.15	11.23	61.21	87.88	1	1
36					1.67	1.67	176.65	---	4.15	7.34	11.69	90.02	85.93	1	1
37					2.0	2.0	239.5	---	4.29	8.36	12.65	120.7	83.77	1	1
38					2.5	2.5	313.8	---	4.21	7.68	11.89	159.6	82.88	1	1
39					5.0	5.0	852.1	---	4.28	6.19	10.47	440.2	79.21	1	1
40					2.0	2.0	205.2	---	0	0	0	94.64	100.0	1	1
41					5.0	5.0	771.5	---	0	0	0	355.9	100.0	1	1
42	A*	0.5000	0.125	0.4375	0.25	0.50	14.72	---	15.17	13.20	28.37	1.32	62.26	1 1/4	1 1/4
43					.25	.625	20.12	---	15.34	12.12	27.46	1.83	59.03	1	1
44					.25	.833	30.51	---	15.51	10.94	26.45	2.81	54.04	1	1
45					.25	1.0	40.41	---	15.64	10.22	25.86	3.75	50.47	1	1
46					.25	1.25	55.54	---	15.73	9.55	25.28	5.19	45.89	1	1

a. Partly blocked emitter.

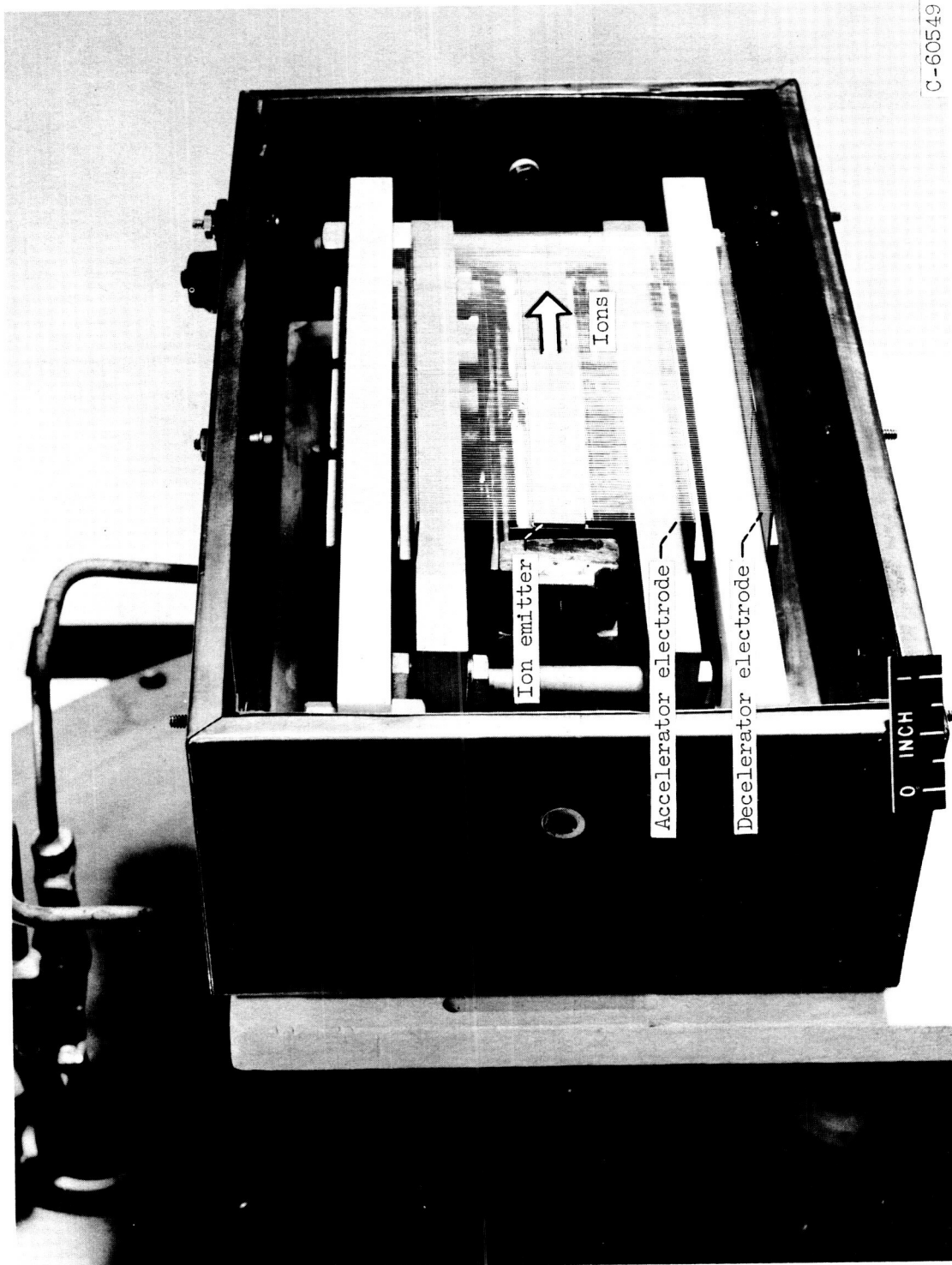


Figure 1. - Ion thruster with closely spaced grid electrodes.

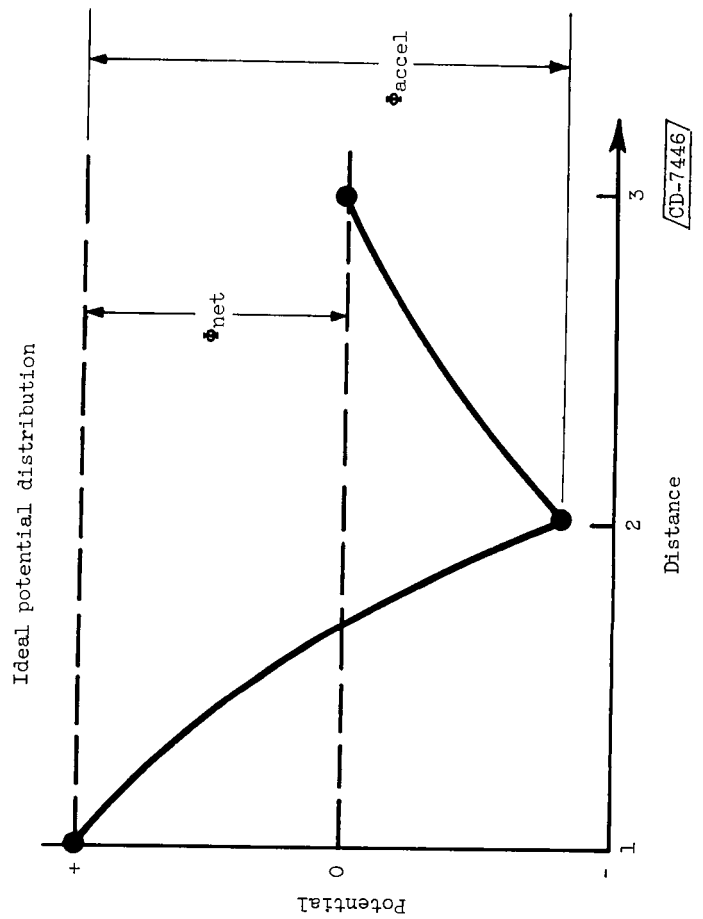
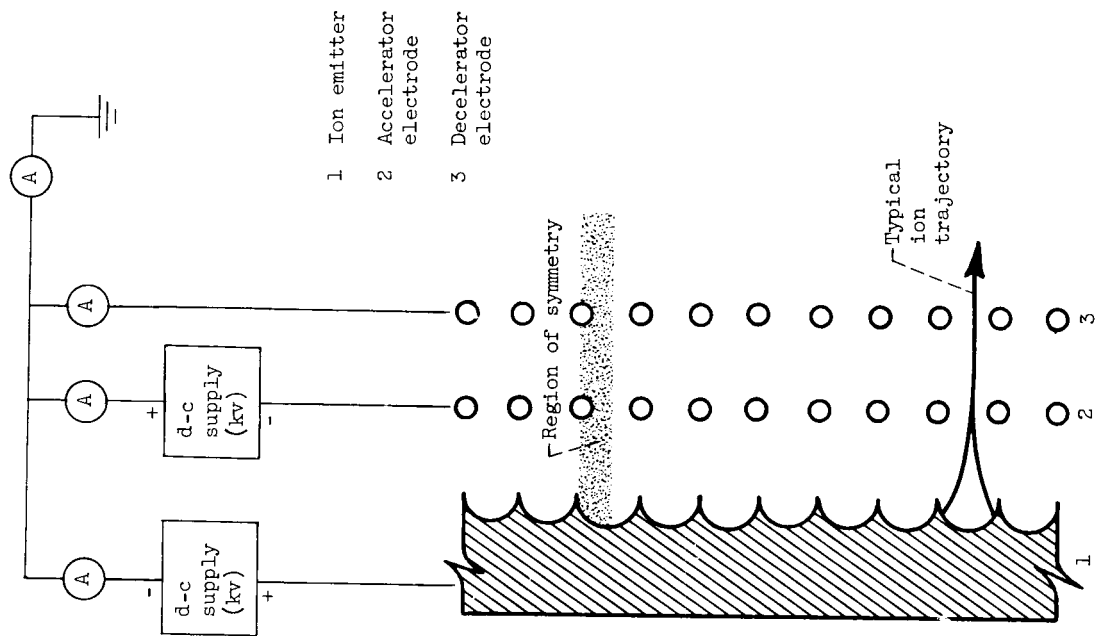


Figure 2. - Section view of portion of ion thruster and ideal potential distribution.

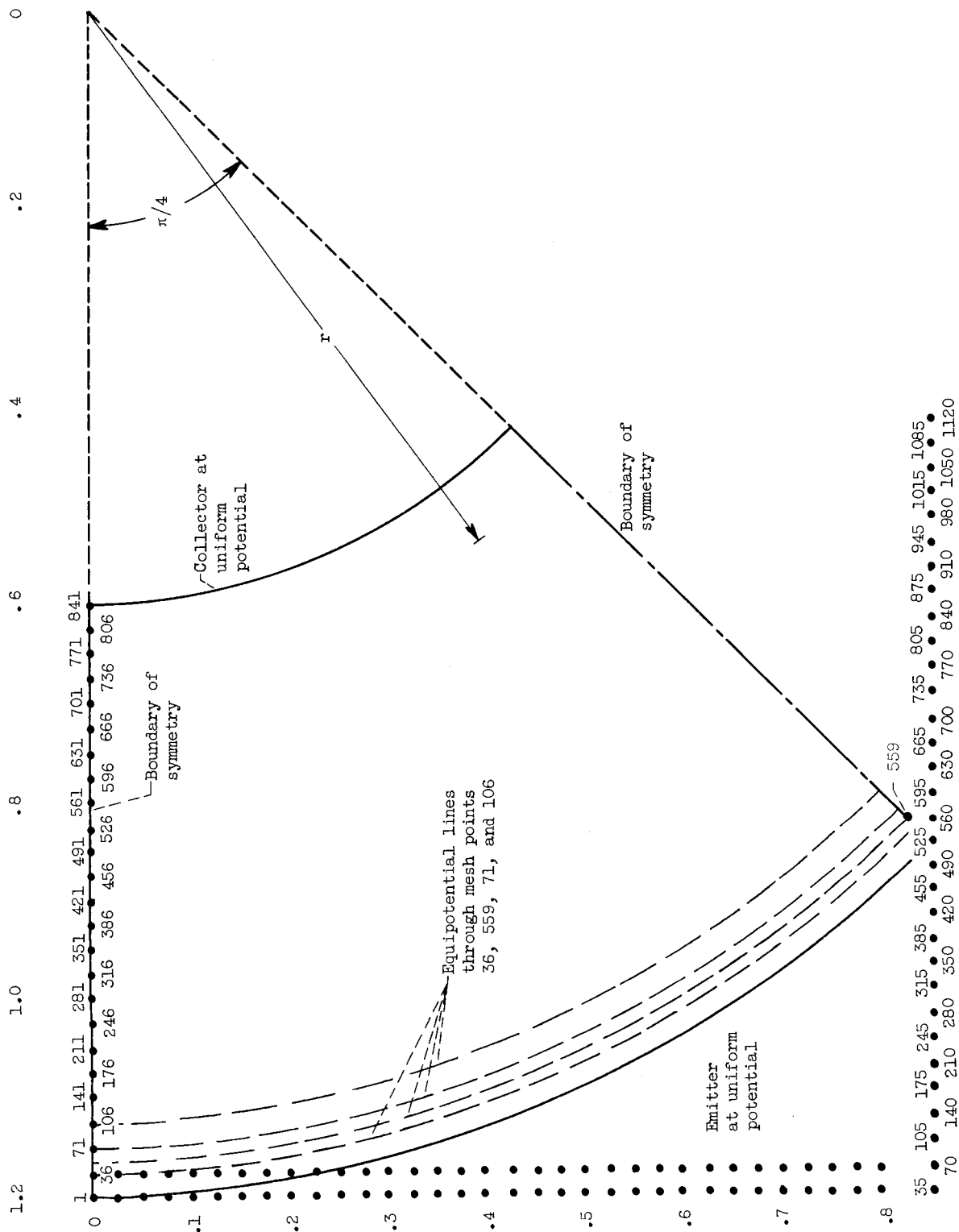


Figure 3. - Sample configuration used for investigation of plane-diode approximation. Emitter radius, 1.2 millimeters; collector radius, 0.6 millimeter; mesh spacing, 0.25 millimeter. Potentials: emitter, 10 kilovolts; collector, 0. Calculated number of mesh points, 695.

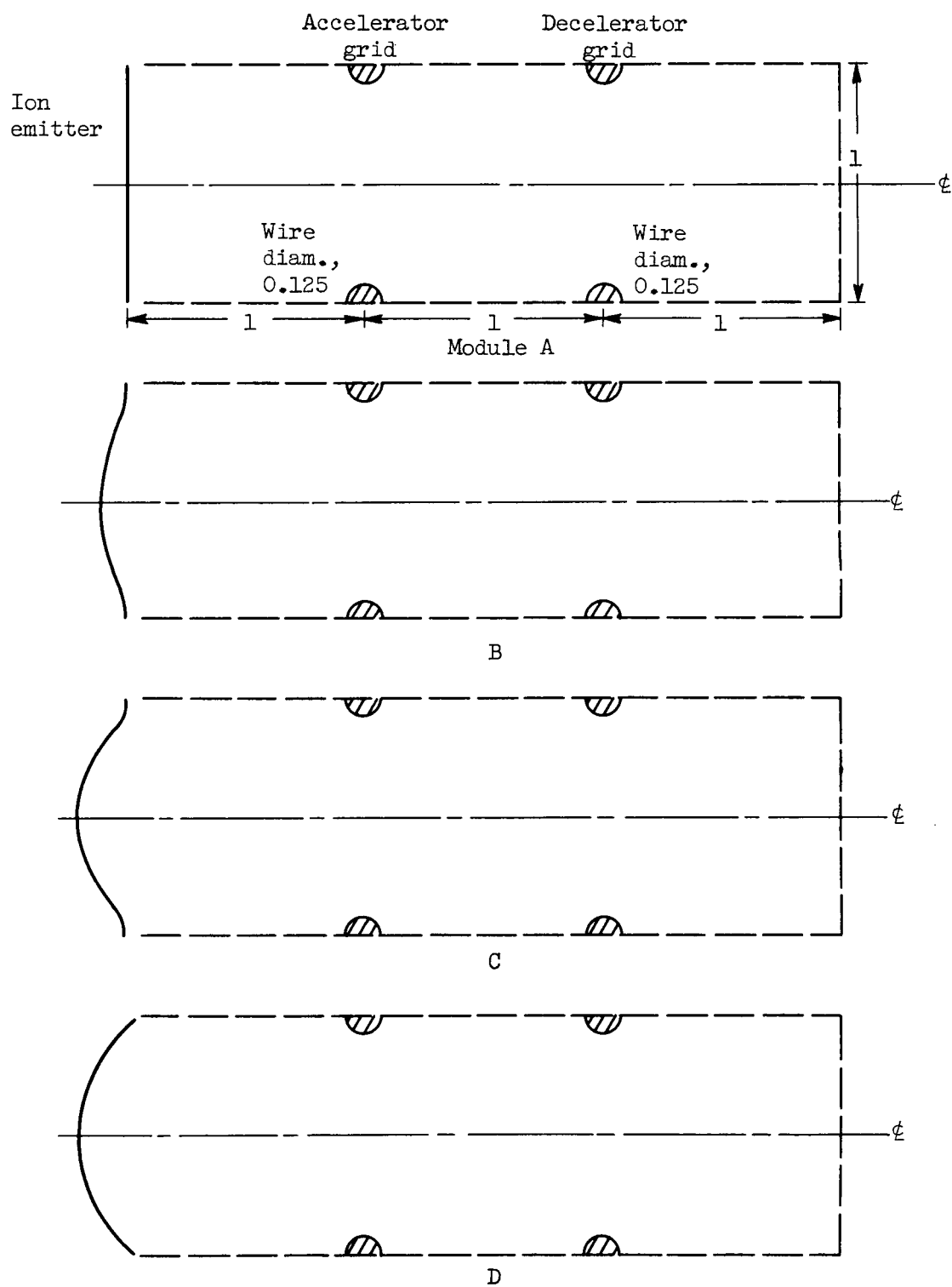
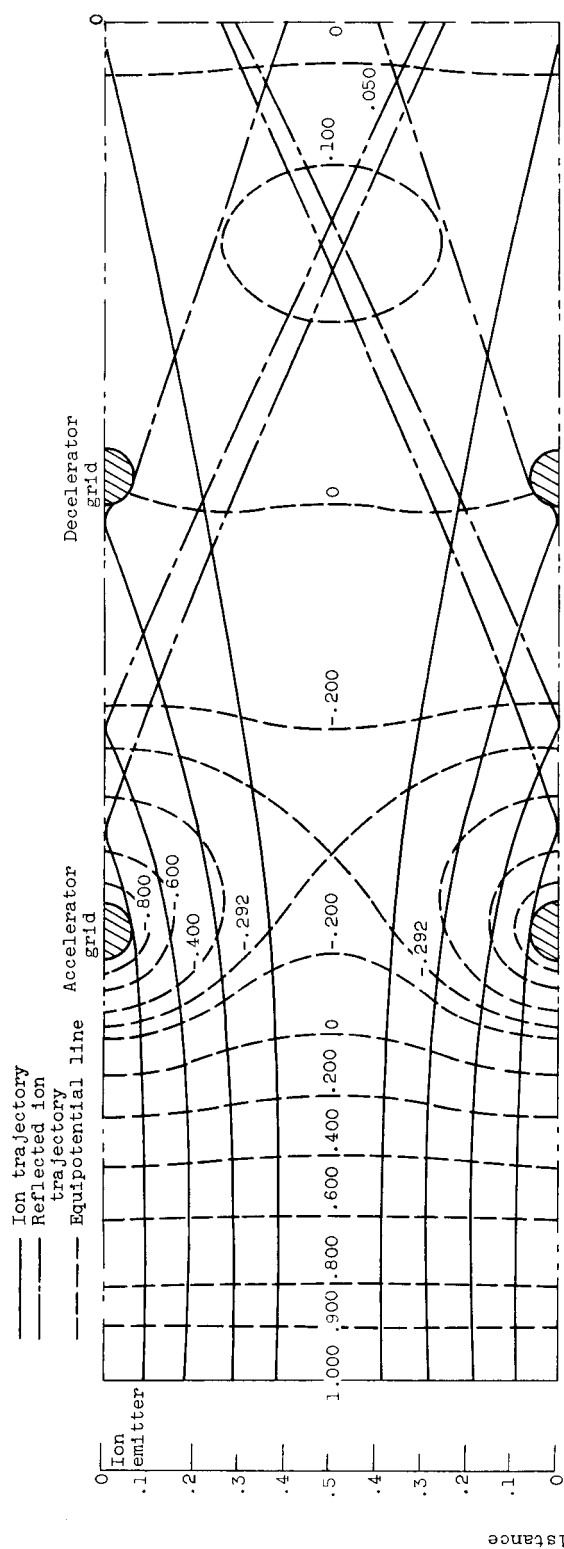
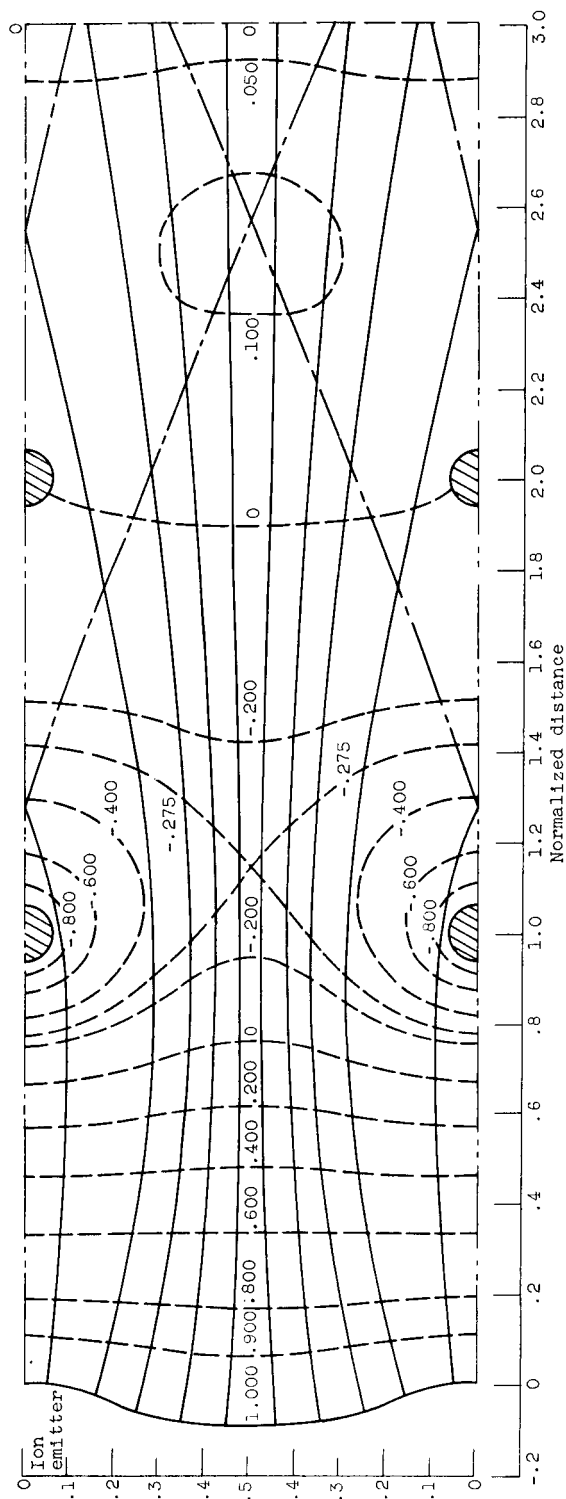


Figure 4. - Sketch of module configurations analyzed. Normalized units; ion-emitter coordinates given in table II.

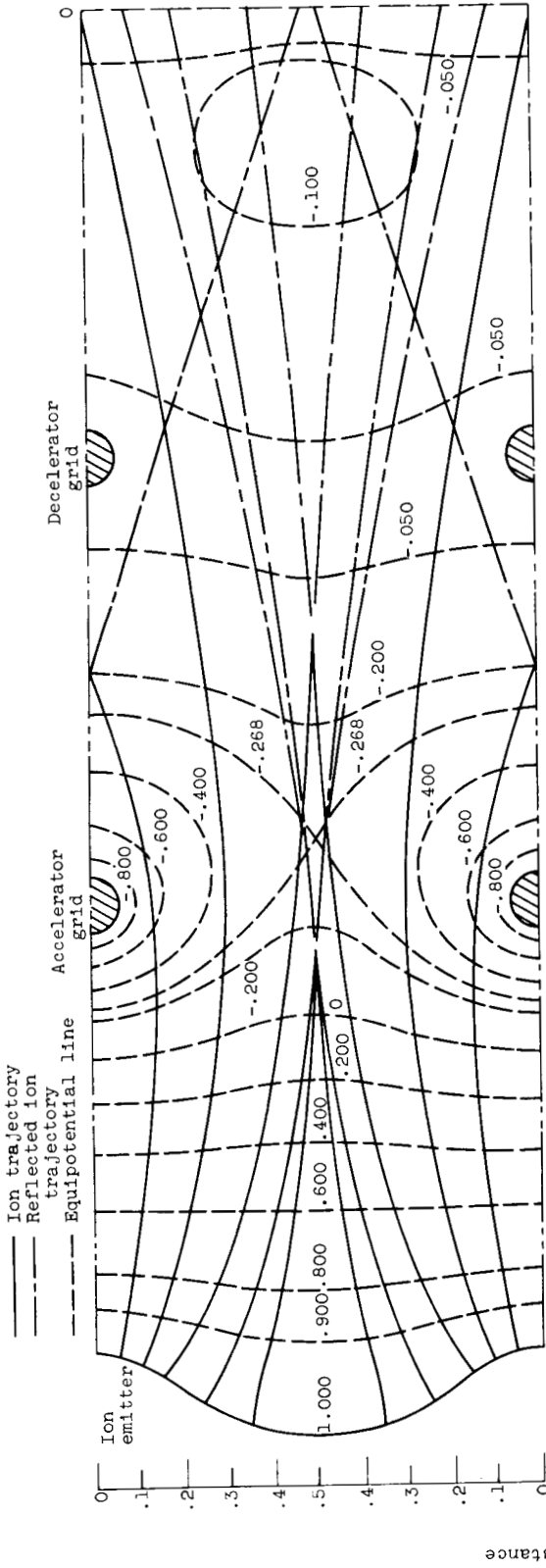


(a) Module A. Average current density at emitter, 341.76 amperes per square meter; percent impingement current: accelerator grid, 19.57; decelerator grid, 10.95; total, 30.52 percent of emitter current.

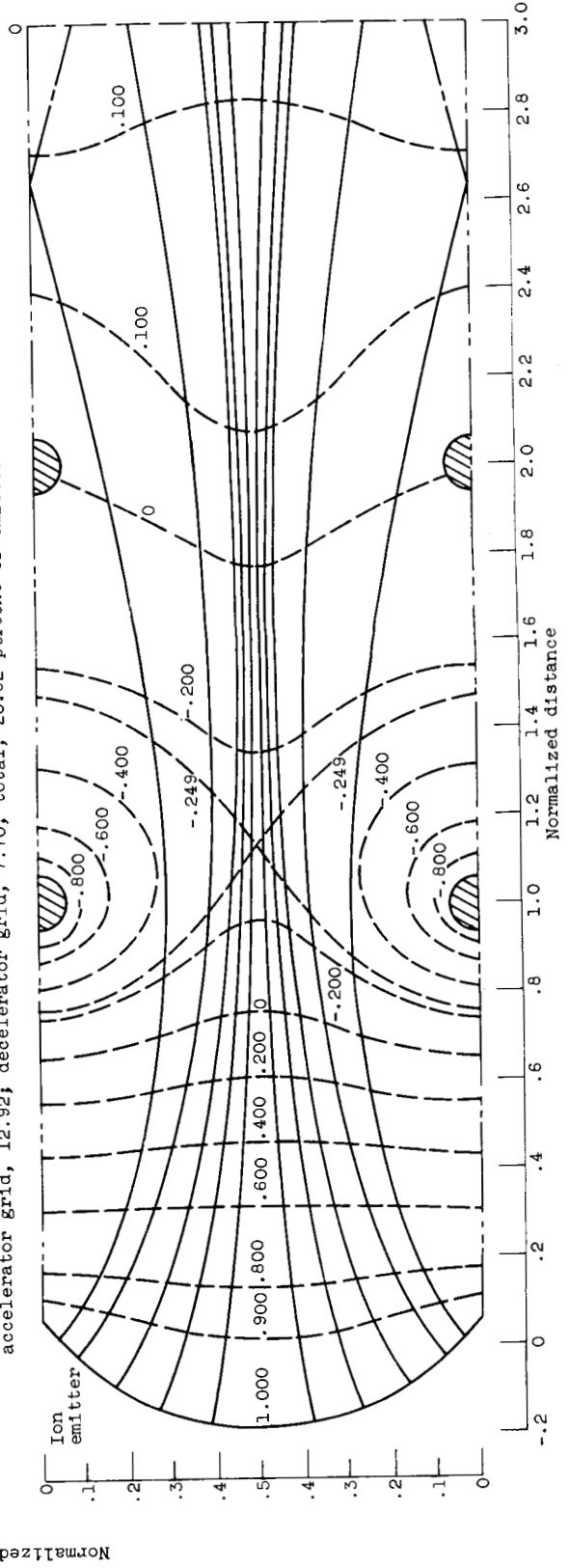


(b) Module B. Average current density at emitter, 512.48 amperes per square meter; percent impingement current: accelerator grid, 14.16; decelerator grid, 8.07; total, 22.23 percent of emitter current.

Figure 5. - Poisson potential distribution and ion trajectories for modules shown in figure 4. Potentials: ion emitter, 1.0 kilovolt; accelerator grid, -1.0 kilovolt; decelerator grid, 0. Wire diameter, 0.125 normalized unit.



(c) Module C. Average current density at emitter, 259.44 amperes per square meter; percent impingement current: accelerator grid, 12.92; decelerator grid, 7.70; total, 20.62 percent of emitter current.



(d) Module D. Average current density at emitter, 239.48 amperes per square meter; percent impingement current: accelerator grid, 4.29; decelerator grid, 8.36; total, 12.65 percent of emitter current.

Figure 5. - Concluded. Poisson potential distribution and ion trajectories for modules shown in figure 4. Potentials: ion emitter, 1.0 kilovolt; accelerator grid, -1.0 kilovolt; decelerator grid, 0. Wire diameter, 0.125 normalized unit.

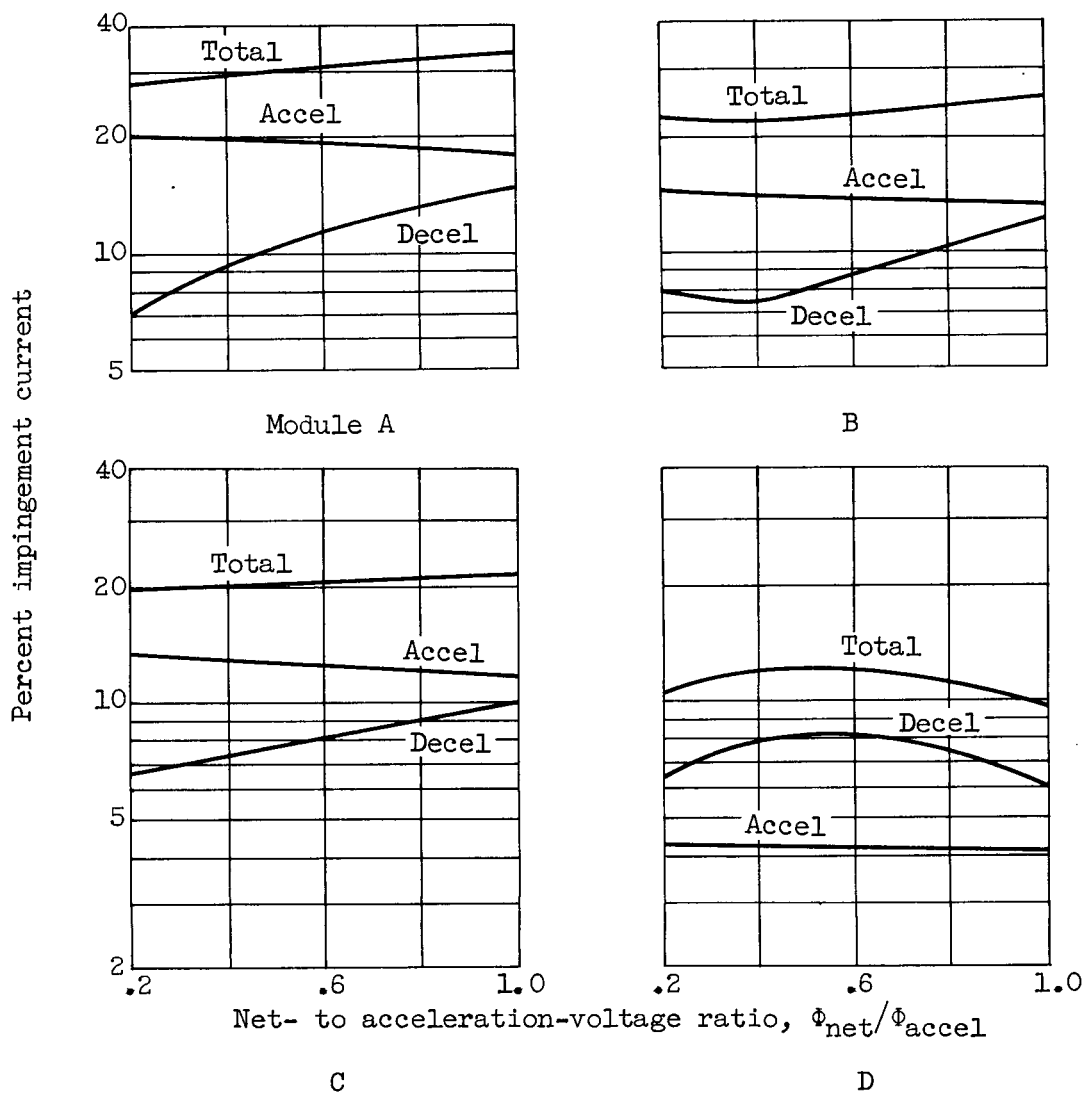
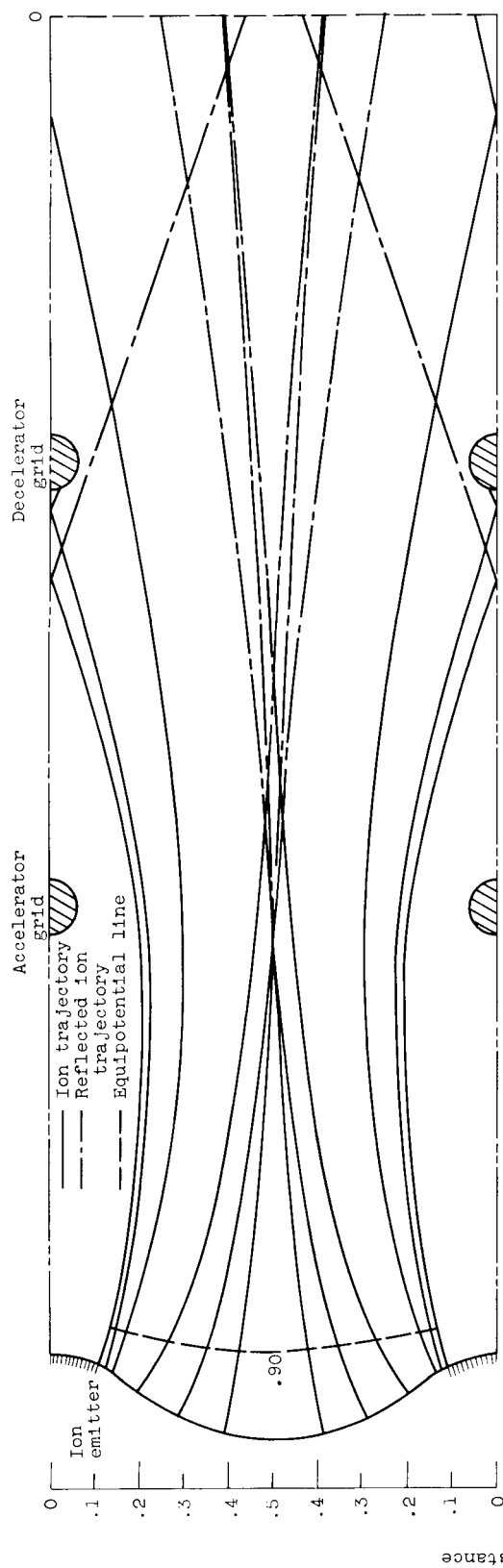
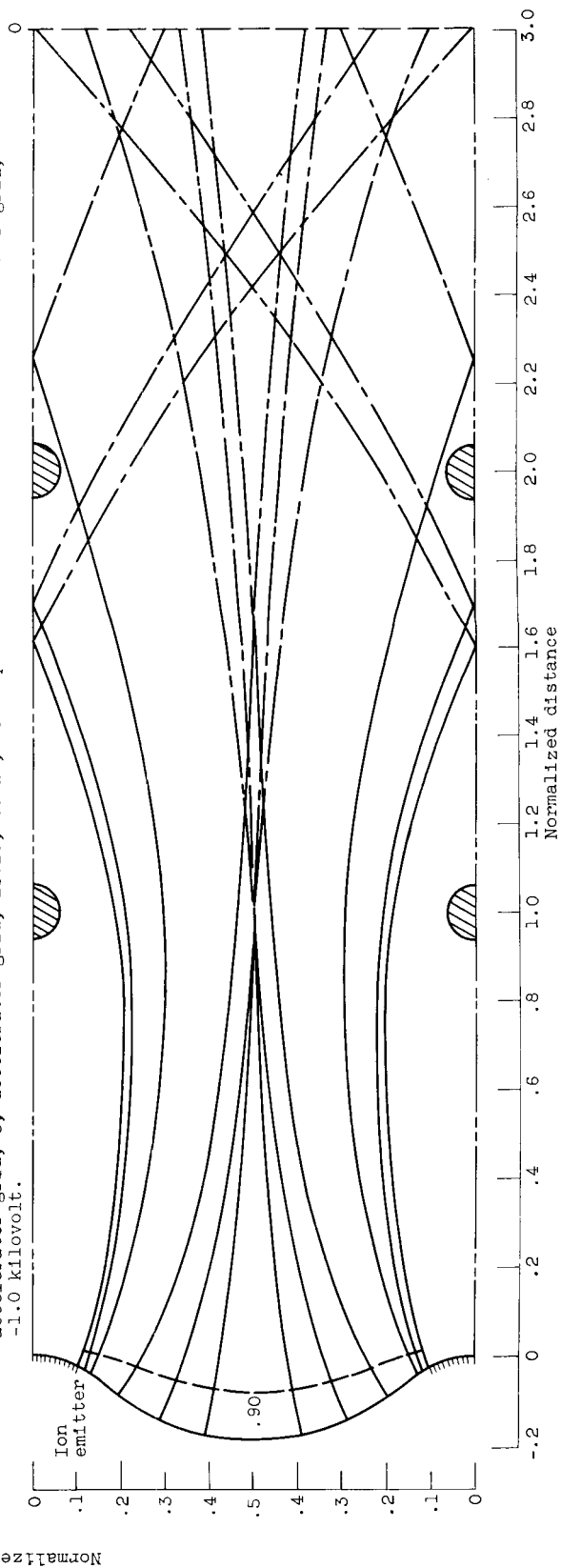


Figure 6. - Variation of percent impingement with net- to acceleration-voltage ratio for modules shown in figure 4.

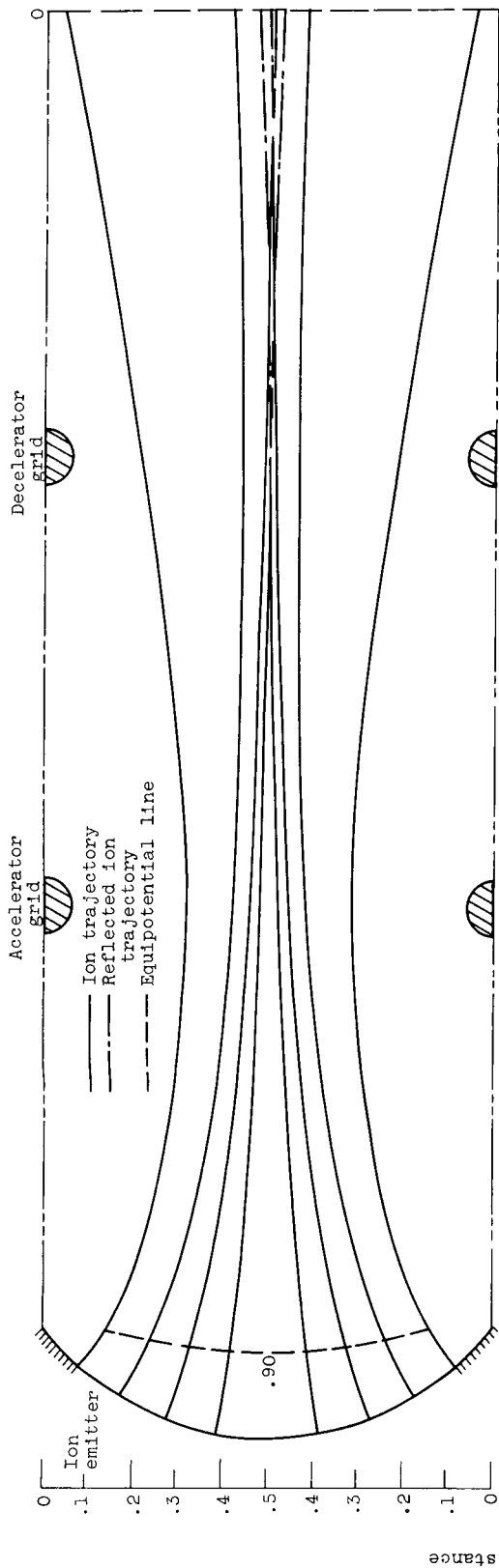


(a) Module C. Average current density at emitter, 239.89 amperes per square meter; percent impingement current: accelerator grid, 0; decelerator grid, 13.15; total, 13.15 percent of emitter current. Accelerator grid, -1.0 kilovolt.

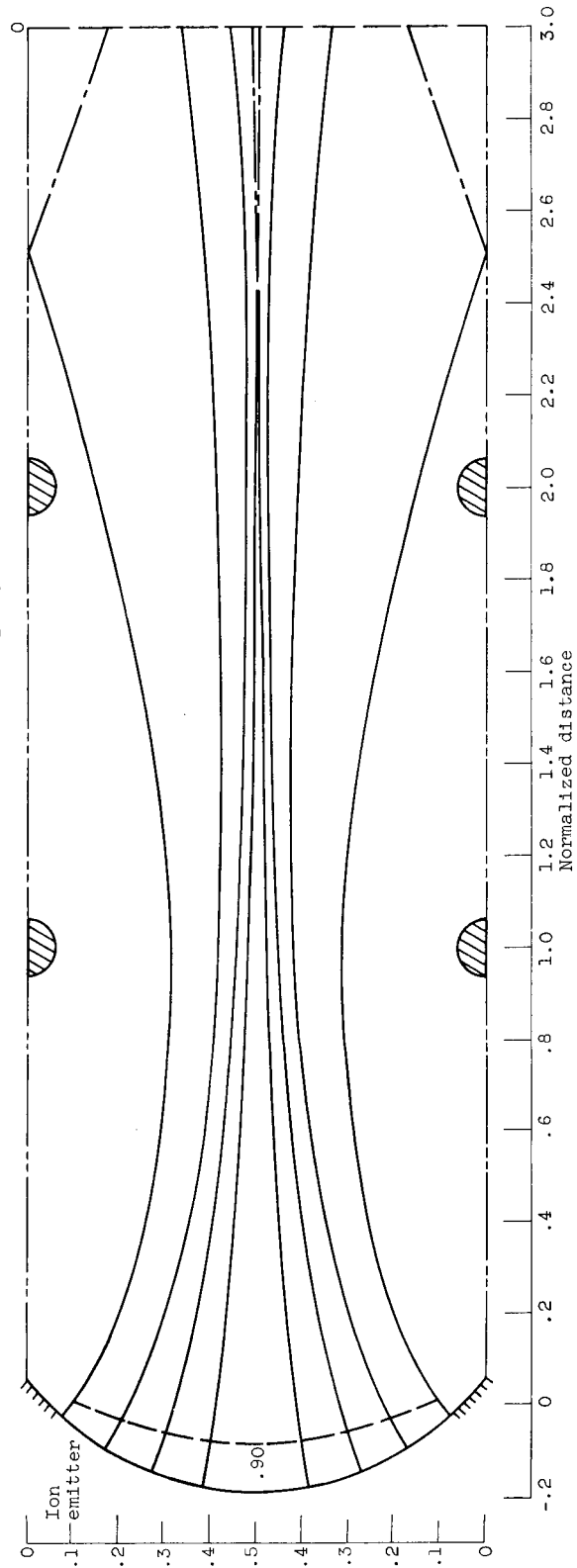


(b) Module C. Average current density at emitter, 900.46 amperes per square meter; percent impingement current: accelerator grid, 0; decelerator grid, 7.72; total, 7.72 percent of emitter current. Accelerator grid, -4.0 kilovolt.

Figure 7. - Effect of partly blocked ion emitter on ion trajectories for modules C and D. Potentials: ion emitter, 1.0 kilovolt; decelerator grid, 0. Wire diameter, 0.125 normalized unit.

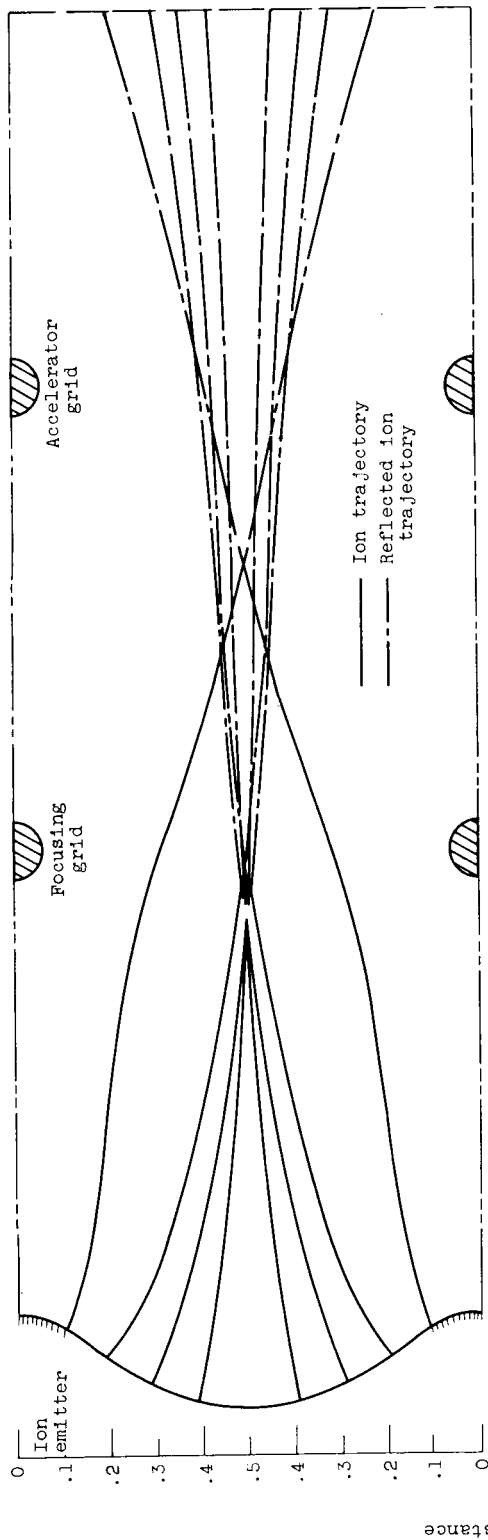


(c) Module D. Average current density at emitter, 205.95 amperes per square meter; percent impingement current: accelerator grid, 0; decelerator grid, 0; total 0. Accelerator grid, -1.0 kilovolt.

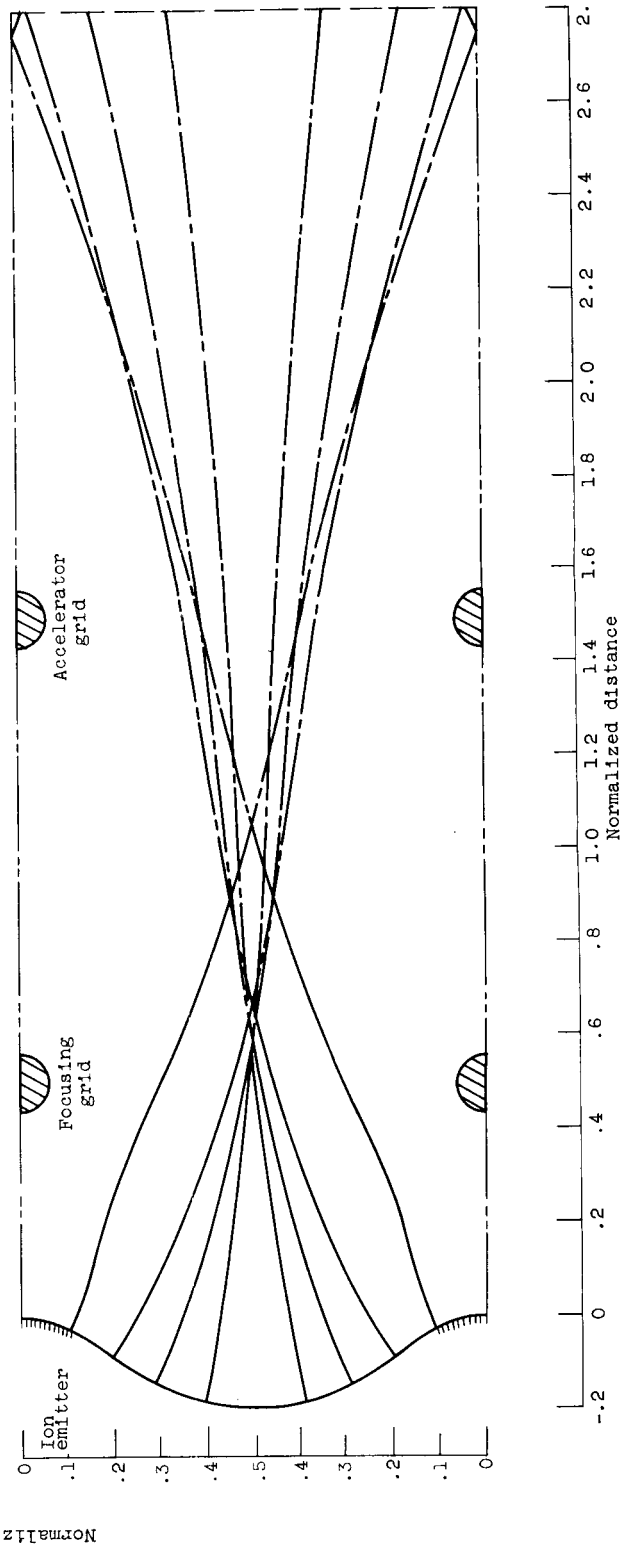


(d) Module D. Average current density at emitter, 777.64 amperes per square meter; percent impingement current: accelerator grid, 0; decelerator grid, 0; total, 0. Accelerator grid, -4.0 kilovolt.

Figure 7. - Concluded. Effect of partly blocked ion emitter on ion trajectories for modules C and D. Potentials: ion emitter, 1.0 kilovolt; decelerator grid, 0. Wire diameter, 0.125 normalized unit.

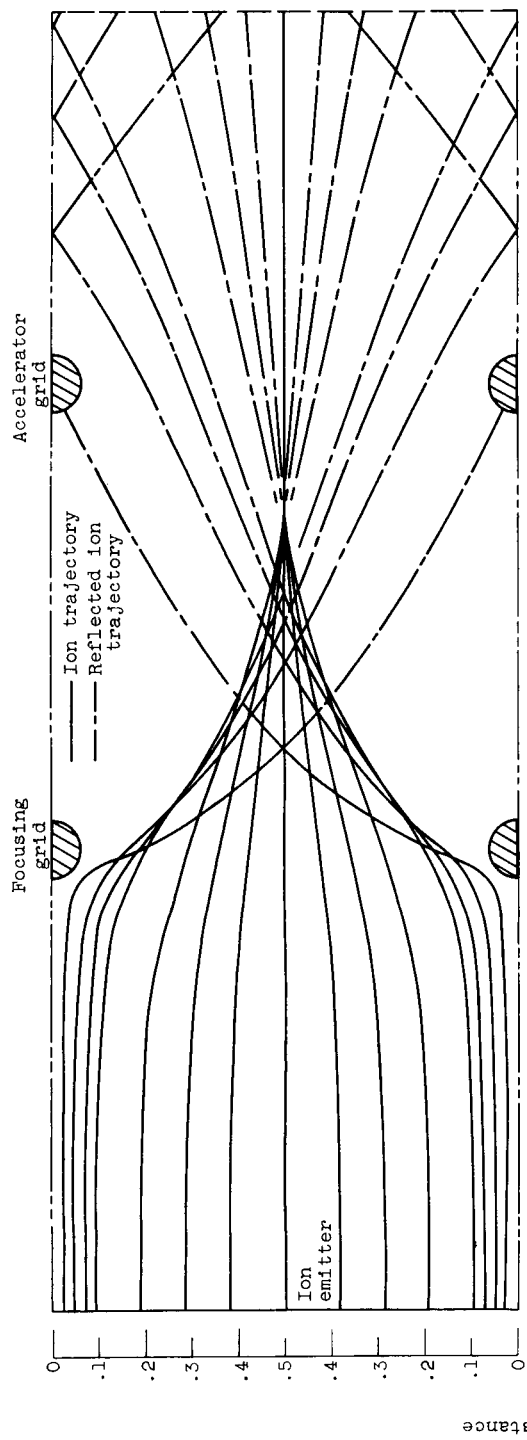


(a) Average current density at emitter, 10.45 amperes per square meter.

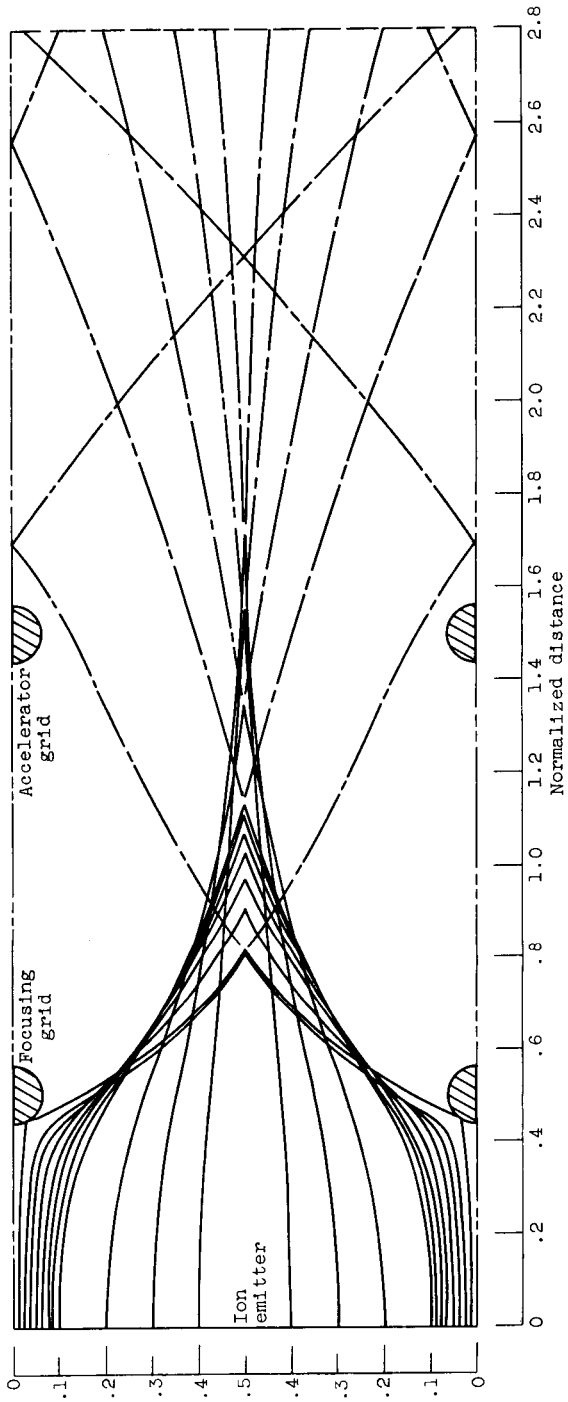


(b) Average current density at emitter, 29.13 amperes per square meter.

Figure 8. - Effect of focusing grid electrode and electrode spacing on ion trajectories of partly blocked ion emitter for module C. Potentials: ion emitter, 1.0 kilovolt; focusing grid, 1.0 kilovolt; accelerator grid, -1.0 kilovolt. Wire diameter, 0.125 normalized unit.

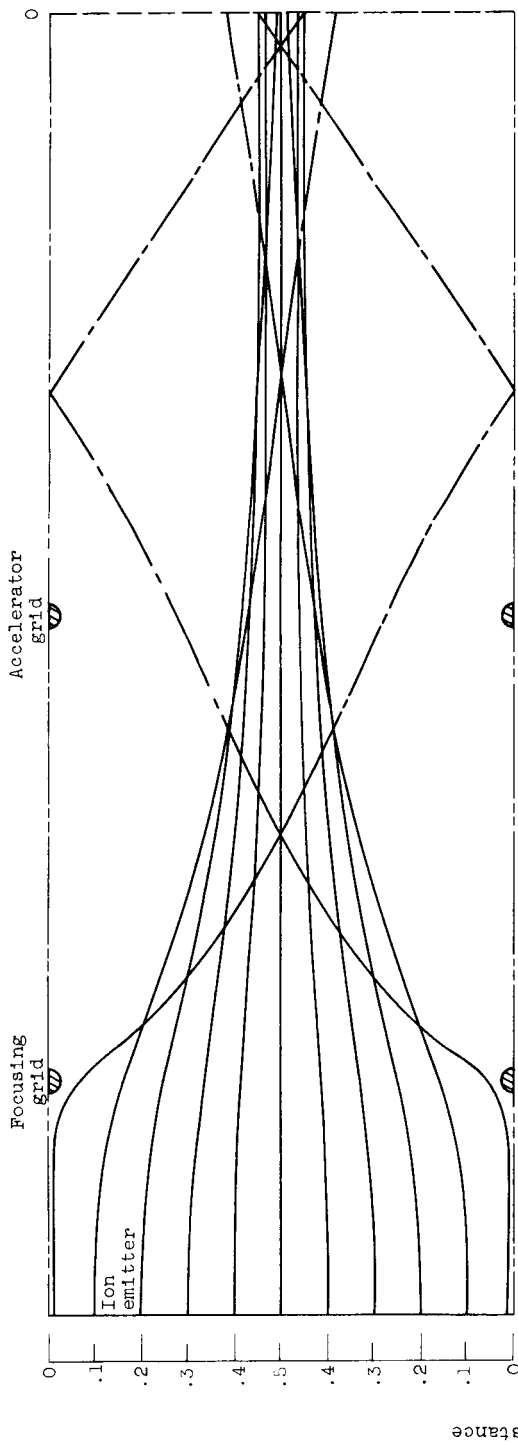


(a) Average current density at emitter, 14.93 amperes per square meter; percent impingement current: focusing grid, 4.56; accelerator grid, 3.10; total, 7.66 percent of emitter current.

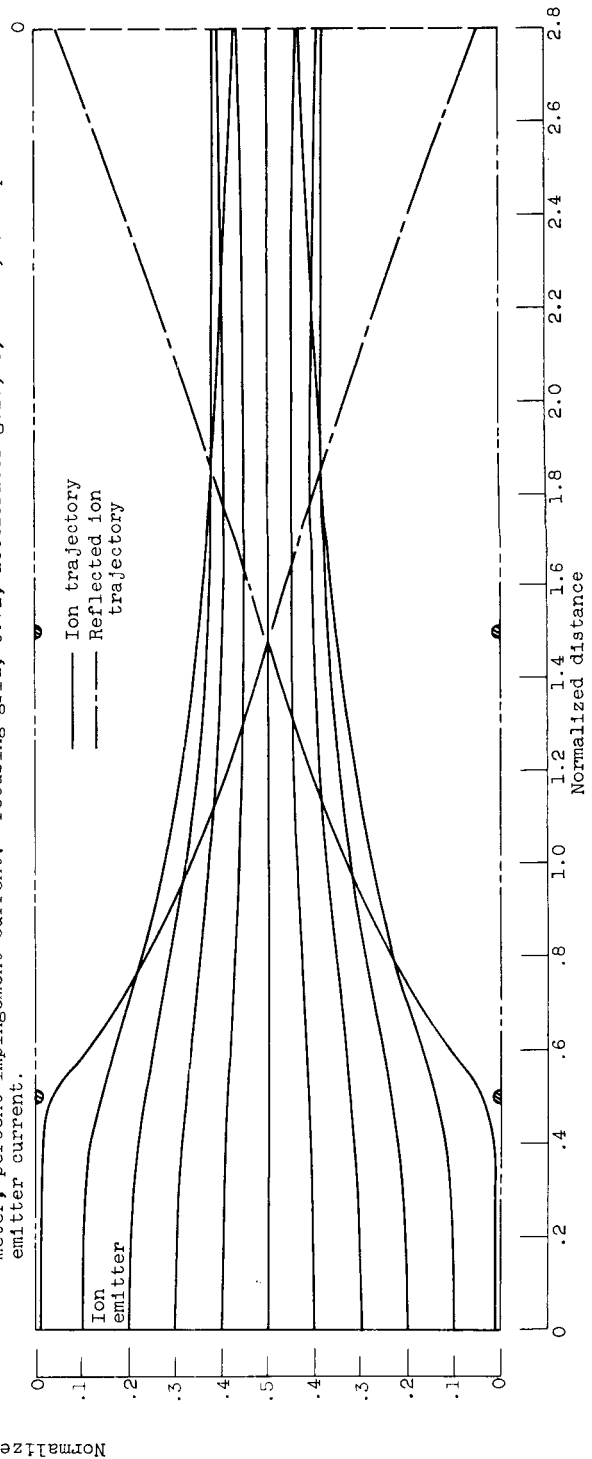


(b) Average current density at emitter, 58.36 amperes per square meter; percent impingement current: focusing grid, 2.56; accelerator grid, 1.00; total, 3.56 percent of emitter current.

Figure 9. - Effect of focusing grid electrode and electrode spacing on unblocked ion emitter for module A. Potentials: ion emitter, 1.0 kilovolt; focusing grid, 1.0 kilovolt; accelerator grid, -1.0 kilovolt. Wire diameter, 0.125 normalized unit.



(a) Wire diameter, 0.050 normalized unit; average current density at emitter, 72.31 amperes per square meter; percent impingement current: focusing grid, 0.72; accelerator grid, 0; total, 0.72 percent of emitter current.



(b) Wire diameter, 0.025 normalized unit; average current density at emitter, 76.60 amperes per square meter; percent impingement current: focusing grid, 0.64; accelerator grid, 0; total, 0.64 percent of emitter current.

Figure 10. - Effect of focusing and wire diameter variation for module A. Potentials: ion emitter, 1.0 kilovolt; focusing grid, 1.0 kilovolt; accelerator grid, -1.0 kilovolt.

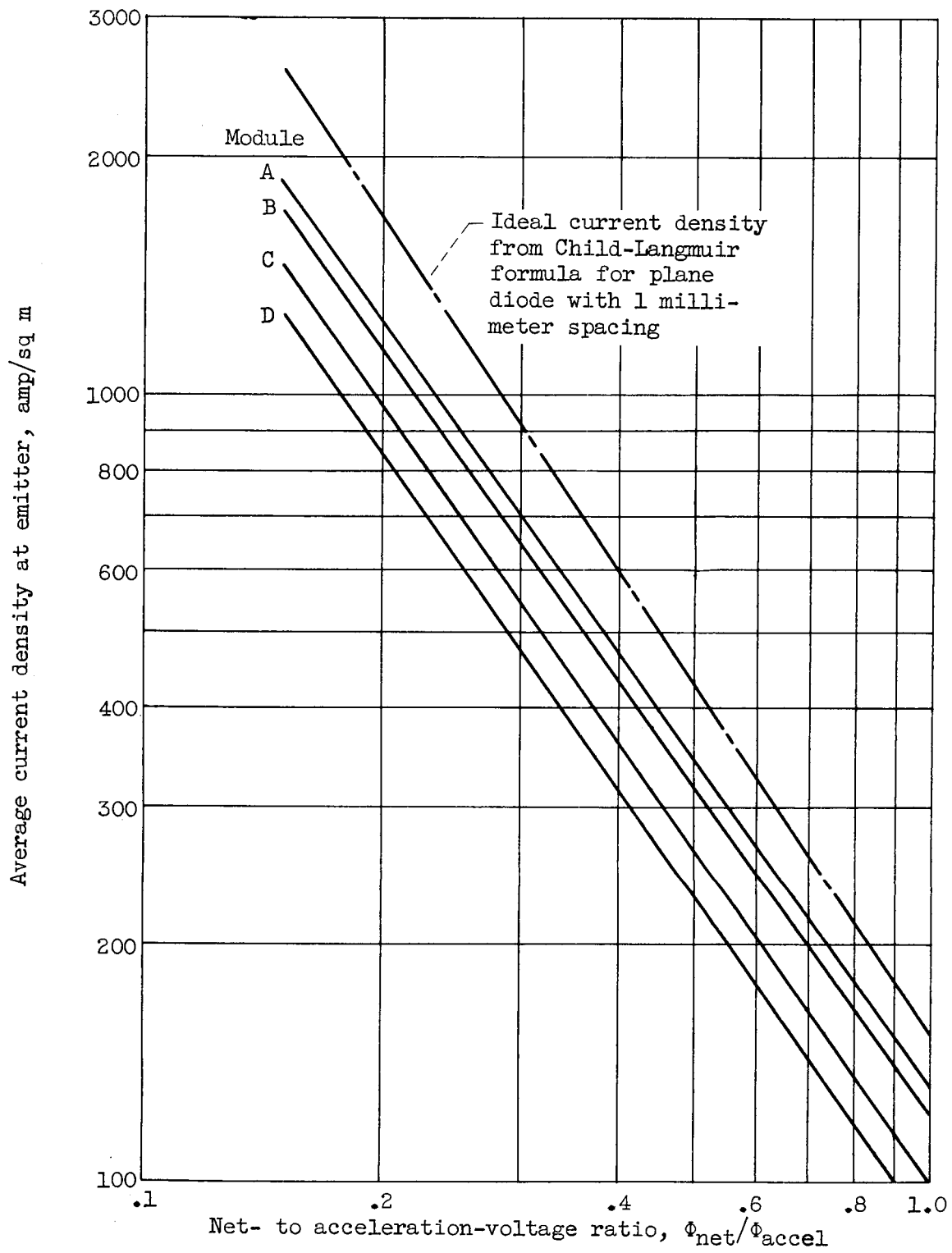


Figure 11. - Variation of current density with net- to acceleration-voltage ratio for modules shown in figure 4. Net potential, 1.0 kilovolt.

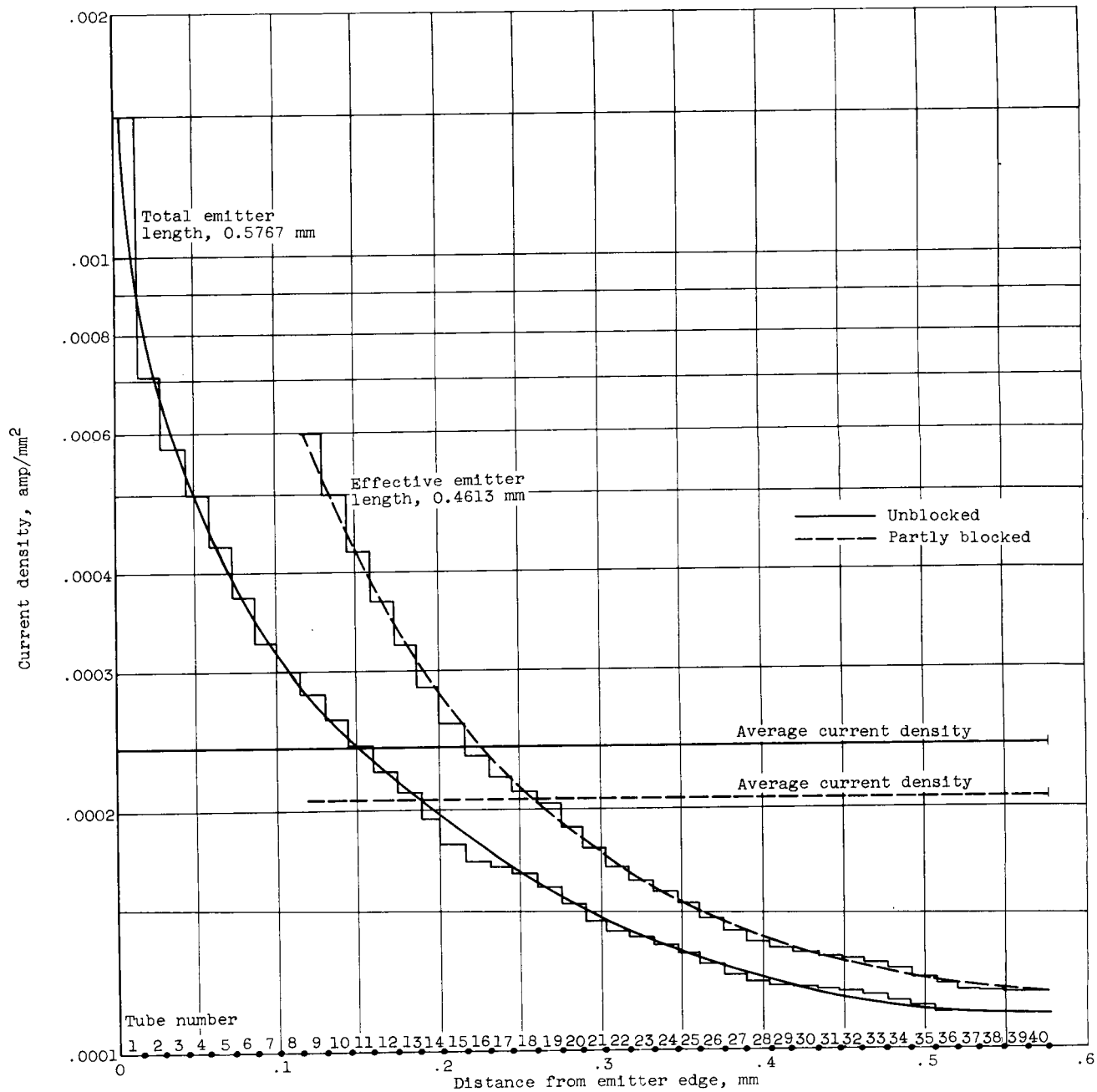


Figure 12. - Current density distribution across emitter for module D. Net- to acceleration-voltage ratio, 0.5; net potential, 1.0 kilovolt.

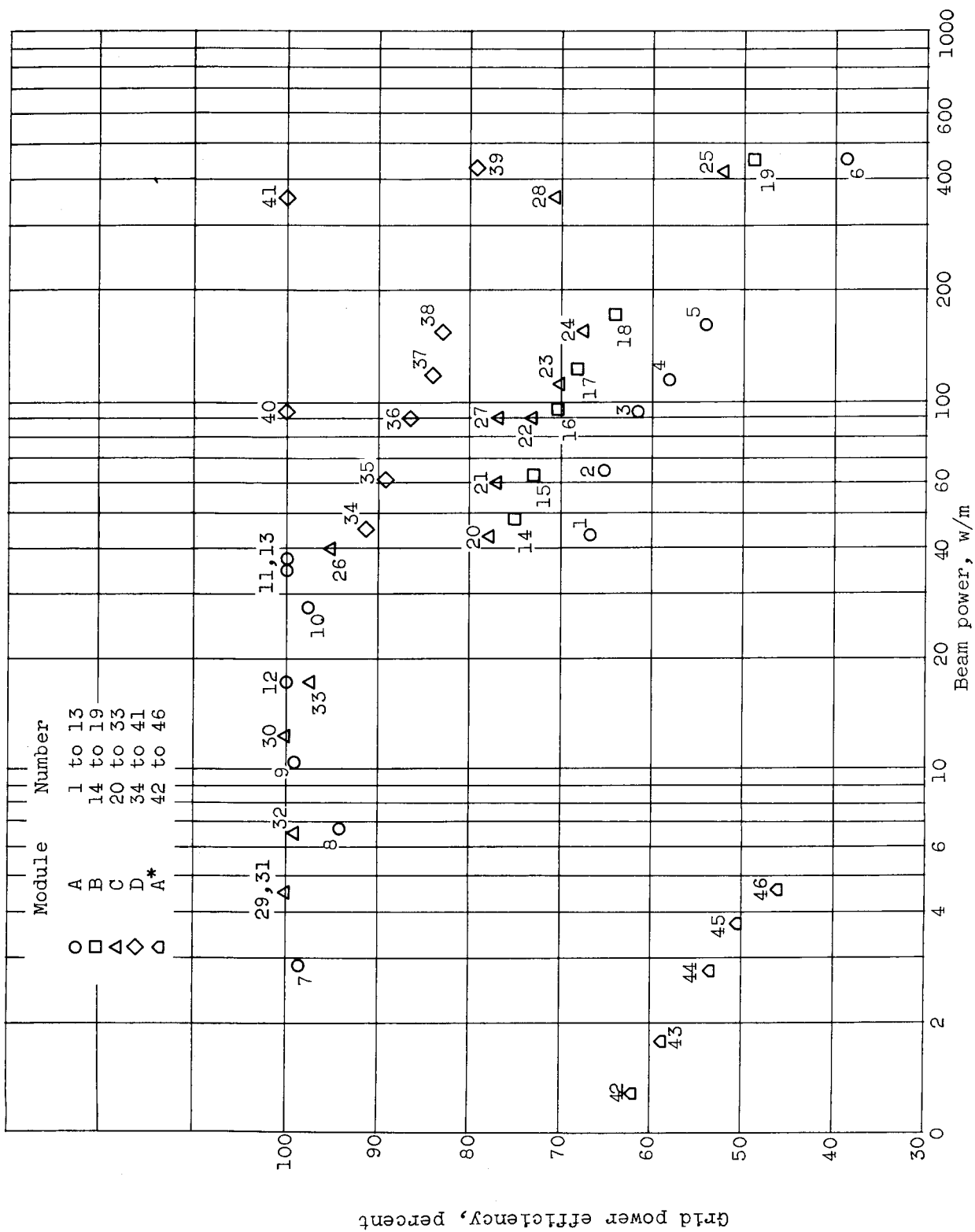


Figure 13. - Summary plot of variation of grid power efficiency with beam power per unit length (z-direction) for all configurations analyzed (see table IV).

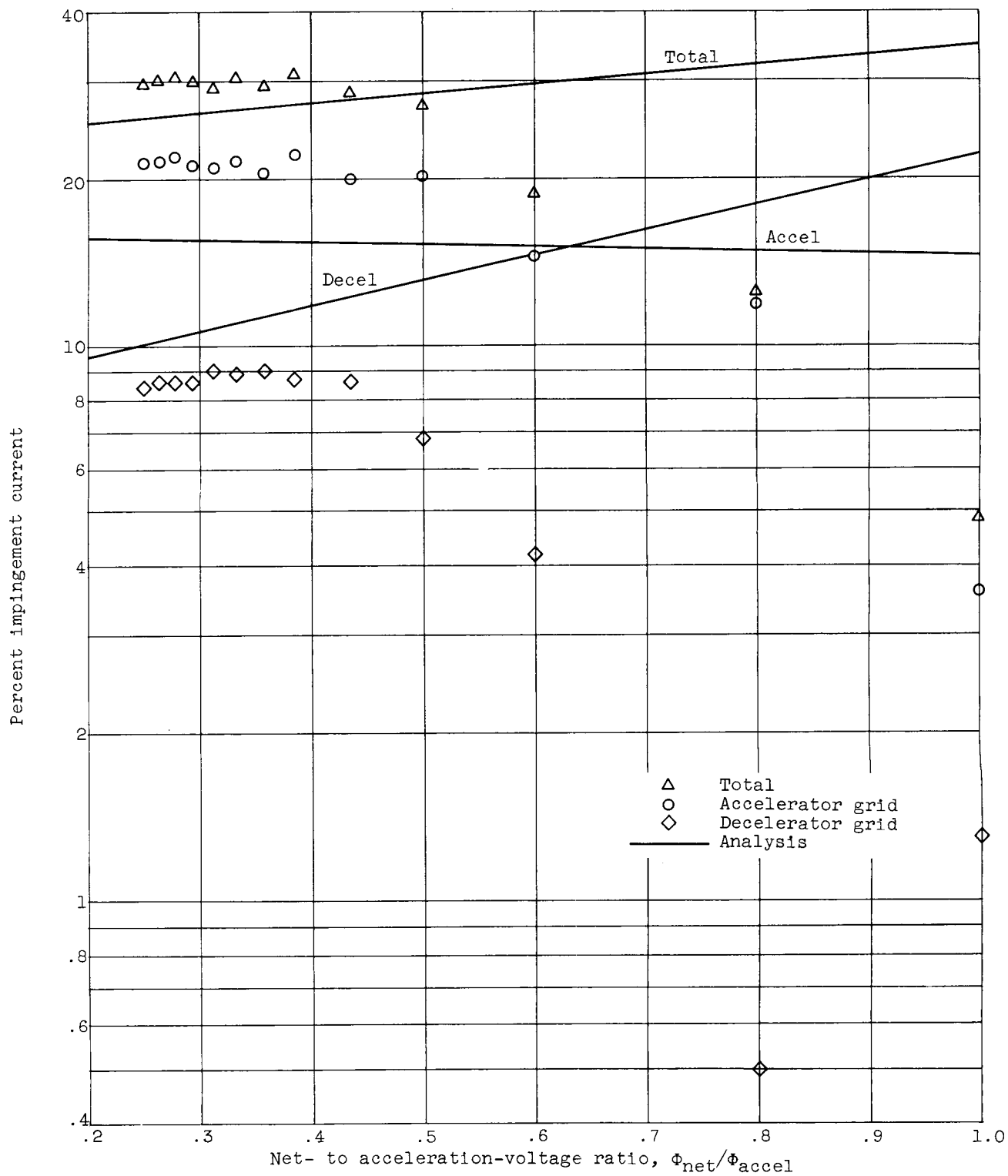


Figure 14. - Comparison of experimental and analytical percent impingement current with net- to acceleration-voltage ratio for Lewis thruster similar to module A.

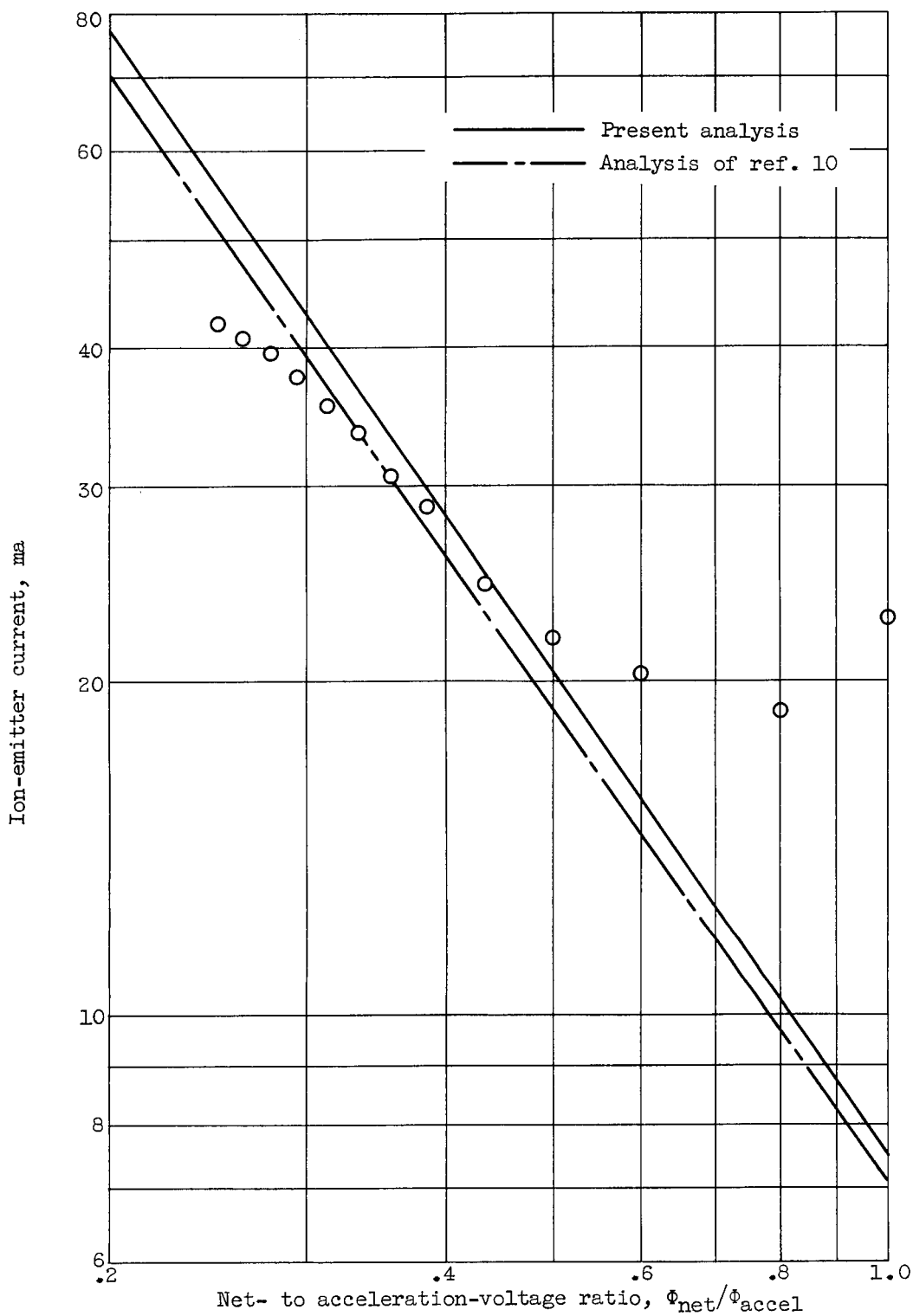


Figure 15. - Comparison of experimental and theoretical ion-emitter currents with net- to acceleration-voltage ratio for Lewis thruster similar to module A. Net potential, 0.25 kilovolt.